UNIVERSITY OF CALIFORNIA

SANTA CRUZ

INTERNAL HEAT:

EXPLORING HOW PLANETARY SURFACES ARE SHAPED

A dissertation submitted in partial satisfaction
of the requirements for the degree of

DOCTOR OF PHILOSOPHY

in

EARTH SCIENCES

by

Jacob Nunes Henriques Abrahams

December 2022

The Dissertation of Jacob Abrahams
is approved:

Professor Francis Nimmo, Chair

Professor Ian Garrick-Bethell

Professor Sonia Tikoo

Peter Biehl

Vice Provost and Dean of Graduate Studies

Contents

List of Figures

Abstract

Internal Heat: Exploring how Planetary Surfaces are Shaped

Jacob Nunes Henriques Abrahams

This thesis consists of three loosely related projects exploring the physics of planetary bodies. The throughline in this research is that I explore how a planetary body's interior influences its exterior – in particular how heat migrating outward drives evolution and leaves detectable traces of that evolution.

Chapter One describes a novel form of volcanism – volcanism on iron bodies, which we call ferrovolcanism. We predict that metallic bodies were able to host volcanism, making metal the third major type of crustal material capable of being volcanic, in addition to ice and silicate planets. We discuss the potential for its observation by the Psyche mission, its role in the evolution of metallic bodies, and its potential influence on the metallic meteorite record.

Chapter Two lays out a way to significantly improve Europa Clipper's ability to measure Europa's global shape, without requiring any extra measurements. By using stellar occultations, measurements that Europa Clipper was already planning to collect, we can supplement radar altimetry to obtain more complete global coverage of Europa. We demonstrated the potential for this combined dataset to significantly improve global fits, which would allow Europa Clipper to better constrain the thickness, rheology, and history of Europa's ice shell.

Chapter Three explores the relationship between rotation rate and tidal dissipation in the interior of Jupiter's moon Io. This is motivated by two separate lines of thinking: 1) Io's volcanoes appear to be offset in longitude from where tidal dissipation models predict they should form, and 2) if a satellite is sufficiently fluid - plausible for Io because it is so strongly heated - it is expected to rotate slightly faster than the synchronous rotation rate we see across solar system satellites. We find that because of the rigidity of its lithosphere, we do not expect Io to rotate nonsynchronously on geophysically relevant timescales.

Acknowledgements

Above all I'd like to thank Francis. He has gone so far beyond what is expected from a PhD advisor. He somehow manages to be both deeply involved in our research and not overbearing or demanding, he is comfortable embracing our independence and willing to provide detailed help, and he combines being bafflingly good at what he does with zero ego. He also has an incredible amount of empathy for grad students, trusting us more than most faculty, paying us better than most, and truly treating us like colleagues. Up to the day I visited Santa Cruz, I assumed I would go elsewhere for grad school. It only took a few minutes of talking to him to realize I really had no choice – I had to come here (I came pretty close to just canceling my next prospective visit, and I did end up cutting it short). I have at many points questioned decisions I've made along my academic career, but I have never doubted that I made the right decision coming here to work with Francis. Thank you.

I also want to thank Ian, who has been an incredible collaborator and mentor. I really appreciate him being both willing to take on a project with me that was too dubious even for Francis (the stoked lunar dynamo), and willing to hand off the reigns to Francis on a project Ian came up with (Io's rotation). Ian has been incredibly helpful along the way, every conversation we have is both fascinating and a ton of fun.

Additional huge thanks to: Myriam Telus and Sonia Tikoo for guiding me through my qualifying exam, and thanks doubly to Sonia for also being on my thesis committee (I'm sorry the lunar project didn't make it into this document, it's still in progress but we will publish it eventually!). Nic Brummell and Jacob Noone Wade for lending some actual quantitative skills to my musing about lunar magmas. Terry Blackburn and Thorsten Kleine for being really fun collaborators early in my PhD. And Joe Kirschvink, Dave Stevenson, and Ben Weiss for being incredible mentors early in my career and the reason I'm here at all. And thank you to Cameron – you wisely avoided the bulk of my PhD, but you've been incredibly helpful toward the end and I can't wait for our adventures going forward.

On the personal side, I wouldn't have been able to do this without my community in Santa Cruz. That centers on Segre House, who welcomed me in, were incredible parts of my life, and

got me through the darker parts of the pandemic. It also forever revolved around the Banana Thugs, who were my first real social outlet in Santa Cruz. Somehow a softball team turned into some of my closest friends, with whom I've broken an ankle and a thumb, traveled to Canada, and spent way too much time thinking about the details of bike components. In addition, the EPS department has always been my anchor. It is an incredible community of kind, brilliant people who are always looking out for eachother. And of course the Planetary people who for some reason shared my fascination with rocks in space – especially folks in A101 who helped me learn the ropes in our department, eventually become a somewhat functional grad student, and goof off when focus got tough. I appreciate everyone who has spent time on bikes with me, whether I was dragging you down trails or up hills that you were afraid of, or you were dragging me down trails or up hills that I was afraid of, and everyone who played racquetball, volleyball, and spikeball with me. Santa Cruz has been filled with amazing people and I am endlessly thankful for the time I got to spend with everyone here.

And of course I want to thank my family. My parents, who never understood my fascination with rocks in space (which started very young) but never stopped supporting it; my siblings Jonah and Emma, who have been kinder and more forgiving than I deserve about me moving and remaining so far away while they were young; and my grandparents, aunts, uncles, and cousins who have just been endlessly positive supporters.

Chapter 1

Ferrovolcanism: Iron Volcanism on Metallic Asteroids

This chapter is a slightly modified reprint of work previously published as: Jacob N. H. Abrahams and Francis Nimmo (2019). "Ferrovolcanism: Iron Volcanism on Metallic Asteroids". In: *Geophysical Research Letters* 46, 2019GL082542. DOI: 10.1029/2019GL082542.

Abstract

Metallic asteroids, the exposed cores of disrupted planetesimals, are expected to have been exposed while still molten. Some would have cooled from the outside in, crystallizing a surface crust which would then grow inward. Because the growing crust is expected to be more dense than the underlying melt, this melt will tend to migrate toward the surface whenever it is able. Compressional stresses produced in the crust while it cools will be relieved locally by thrust faulting, which will also provide potential conduits for melt to reach the surface. We predict iron volcanism to have occurred on metallic asteroids as they cooled and discuss the implications of this process for both the evolution and the modern appearance of these bodies.

1.1 Introduction

Three major types of crustal material are observed in the solar system. The most familiar, silicate crust, is found on the terrestrial planets and their moons, most asteroids, and on Io. The other common type of crust is formed from ices, primarily water ice, on the surfaces of most outer solar system moons, some asteroids, and most Kuiper belt objects. In addition to ice and silicates, a less common third type of crust is present in the solar system: metallic core material left behind following collisional disruption of the mantle of a differentiated body (Asphaug et al. 2006; Yang et al. 2007). These bodies have been detected in the asteroid belt (Matter et al. 2013; Neeley et al. 2014) and contribute substantially to the meteorite record (Hutchison 2004). However, our understanding of their surfaces is very limited – the first detailed images of a metallic asteroid will come from the Psyche spacecraft, which is scheduled to launch in 2022 (Lord et al. 2017).

Volcanism occurs throughout the solar system in a variety of different forms (e.g. Lopes and Gregg 2004; Wilson 2009). All terrestrial planets (and Io) exhibit silicate volcanism, and a number of icy bodies display either geomorphic signs of cryovolcanism (Moore 2001; Schenk et al. 2001) or directly observed plume behavior (Porco et al. 2006; Roth et al. 2014). In this paper we explore the question of whether metallic bodies can host their own novel style of volcanism. Metallic volcanism should bear most resemblance to silicate volcanism, where the melt is buoyant relative to the solid matrix. This is in contrast to cryovolcanism, where the melt is more dense and mechanisms other than buoyancy are needed to aid its ascent (e.g. Manga and Wang 2007; Crawford and Stevenson 1988). The main differences between iron volcanism and silicate volcanism are the lower viscosity of liquid metal, the higher ductility of solid metal, metal's higher resistance to fracture and the likely absence of a low-density crust able to stall fluid migration. In addition, our analysis is concerned with a body hosting an iron 'magma ocean', where the entire interior is molten, rather than broad regions of low melt fraction or magma confined to small chambers.

All but the smallest differentiated bodies will have partially molten iron cores for at least the first ∼100 million years of the solar system, the period in which their mantles are most likely to be removed (Bottke et al. 2005). When a fully molten core is then exposed to space, it will rapidly form a quench crust on the surface. This new crust will either sink, exposing

new melt to space and rapidly freezing the whole body, or it will be supported by its own strength and crystallize slowly from the outside in. Crucially, observations of cooling rate-Ni correlations indicate that some asteroid bodies crystallize from the outside-in (Yang et al. 2007; Yang et al. 2008; Chabot and Haack 2006), which is the mode of solidification of interest to this work. These observations show that, within the IVA meteorite family, the samples with the fastest cooling rates have the lowest incompatible element contents, implying that the shallowest material crystallizes first i.e. top-down solidification. For the purpose of this paper we accept this empirical observation; further aspects of solidification are addressed in Scheinberg et al. (2016) and Neufeld et al. (2019). Proceeding with the assumption that bodies with self-supporting solid crusts occur, we predict that in such bodies the buoyant melt beneath the crust will periodically be able to erupt, influencing their cooling and creating volcanic features on the surface.

The aim of this manuscript is to investigate the basics of metallic volcanism. Because iron volcanism is a novel concept, and many of the important parameters are poorly constrained, we take an order-of-magnitude approach whenever possible and are only seeking to make approximate predictions for the real behavior. First we discuss the thermal and mechanical evolution of an initially molten metallic asteroid. Then we address the ability of melt to reach the surface and challenges to that migration. We conclude by discussing some features of how metallic volcanism may present itself, and the need for continuing work anticipating its morphology, looking for it in current records, and collecting additional data.

1.2 Thermal Evolution

1.2.1 Thermal evolution prior to disruption

Bodies formed in the first ∼2.5 Myr of the solar system will possess enough short lived radionuclides, particularly ^{26}Al, to melt and separate metals and silicates (Goldstein et al. 2009; Hevey and Sanders 2006). In the absence of mantle convection (Tkalcec et al. 2013) or silicate melt advection, the core will not begin to cool significantly until a conductive cooling wave has propagated to the base of the mantle. For a thermal diffusivity of $\approx 10^{-6}$ m^2/s (Carslaw and Jaeger 1959), even a 60 km mantle has a thermal timescale of 100 Myr. Since 16

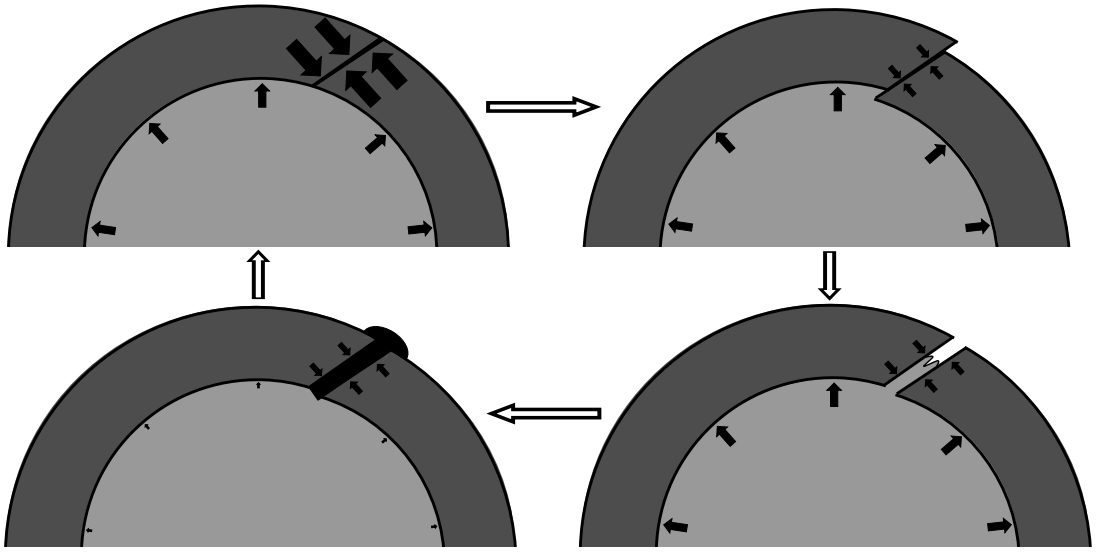

Figure 1.1: Cartoon depicting the volcanic cycle we describe. Beginning in the top-left is the typical state of the crust, where compressional stress prevents the melt at depth from reaching the surface. Volcanism then begins with a faulting event and the resulting decreased local compressional stress in the crust is no longer larger than hydrostatic pressure. Next, the liquid interior forces open the fault and melt migrates through the newly formed dike. Finally, melt reaches the surface and the now-depressurized ocean is no longer able to support the crust, causing the crack to close again. Subsequent crustal growth increases contraction in the crust slowly until faulting can occur again.

Psyche, the largest metallic asteroid, has an average radius over 100 km (Shepard et al. 2017) its mantle thermal timescale prior to disruption will have exceeded this value. Because disruption most likely occurred during terrestrial planet accretion (Bottke et al. 2005), the cores of proto-Psyche and other similar-sized asteroids will have been molten when disruption occurred.

1.2.2 Thermal evolution after disruption

After disruption (and any requisite reaccretion, which will be rapid - on orbital timescales) the body of interest will be a molten, hydrostatic spheroid exposed to space. Initially, a quench crust will form very rapidly–a millimeter thick crust can form in ∼minutes–but crustal growth slows down substantially once conduction replaces radiation as the rate-limiting step. Preventing fresh crust from immediately sinking until a self-supporting crust can form is

beyond the scope of this paper, but as discussed in Section 1.1, the meteorite record shows that this took place on some metallic bodies. Moreover, crystallization from the top down, rather than from the bottom up, is expected based on the expected liquidus and adiabat slopes (Williams 2009). Once a strong crust forms, in the absence of core superheat and volcanism its thickness h will grow according to the Stefan solution (Turcotte and Schubert 2014), approximated by $h \approx 20$ km$(t/1$ Myr$)^{1/2}$. For these very approximate values, the time to form a 20 km crust is roughly one Myr.

This evolution can be more complicated if the simple top-down conductive cooling of the Stefan problem does not apply (Scheinberg et al. 2016). Advection is one way to modify this picture, but as discussed later fluid eruption is not expected to significantly alter the thermal behavior. Delamination at the base of the crust can also modify the thermal evolution of the body by maintaining a thinner crust. However, although delamination is likely to occur, Neufeld et al. 2019 show that neither it nor core superheat significantly modify the overall thermal evolution of the body, and that the Stefan assumption is generally justified.

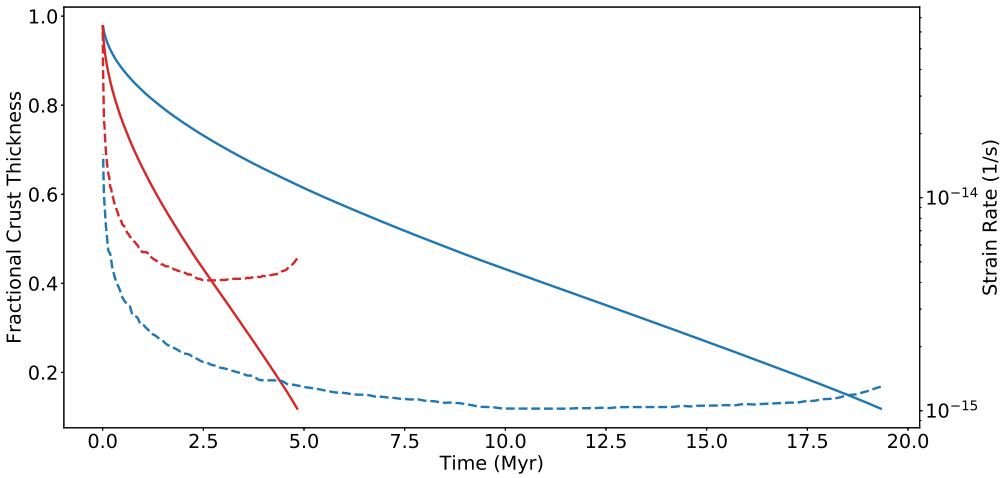

Figure 1.2: Evolution of an initially molten spherical iron body. Solid lines show the thickness of solid crust as a fraction of body radius and dashed lines show smoothed strain rate due to surface contraction. Red lines are for a 100 km radius body and blue lines are for a 200 km radius body. This model uses the approach of Nimmo and Spencer (2015) to numerically solve the Stefan problem with the surface pinned to 200 K, the liquid interior at 1200 K and other parameter values given in Table 1.1. Models taking core superheat and delamination into account (Neufeld et al. 2019) yield similar results

.

1.3 Volcanic Cycle

Having discussed thermal evolution, we now move on to a discussion of how metallic volcanism would arise. The eruption process we describe takes place in three major stages, depicted in cartoon form in Figure 1.1. As the crust solidifies, the decrease in volume associated with the phase change results in radial contraction and compression. The second stage occurs when this stress exceeds the friction on existing faults, those faults move, and local low-stress regions surrounding the faults arise. The interior melt is then able to force open these cracks and migrate through them. The third stage describes when the liquid interior, which now has a decreased volume, causes sufficient contraction to close the cracks again and re-establish local compression.

1.3.1 Stage 1: Stress evolution due to bulk solidification

New solid will occupy a smaller volume than the melt from which it formed, and the resulting radial contraction generates compression. The deeper, hotter solid (the deeper ∼half of the crust) will be ductile and able to viscously relax away this stress, while the colder upper layers will either deform elastically or undergo brittle failure. Because the crust will be in compression, volcanism will tend to be suppressed. To erupt, melt needs to force open cracks which are being held together by compressive stresses. It is important to note that both Mercury and the Moon host volcanism despite globally compressive stress environments (Head and Wilson 1992; Klimczak et al. 2018), so silicate volcanism can - at least locally and temporarily - overcome compression.

For a nominal 10 km crust with a linear thermal gradient, that gradient is $\frac{dT}{dz} \approx 10^{-1}$ K/m. This corresponds to a radial contraction (due to crystallization) of $\dot{h}\frac{\Delta\rho}{\rho} = \frac{k\frac{dT}{dz}}{L\rho}\frac{\Delta\rho}{\rho} \approx 10^{-10}$ m/s, where L is latent heat and k is thermal conductivity. Note that part of the contraction is due to the entire crust cooling as the thermal profile gets longer, which has a similar magnitude to the contraction due to crystallizing so we fold it into our already very approximate $\Delta\rho$. This volume loss corresponds to a strain rate of $\dot{\epsilon} = \dot{h}\frac{\Delta\rho}{\rho}/R \sim 10^{-15}$ s^{-1}. This strain rate will evolve substantially with the crustal thickness; output from a simple numerical model of solidification-derived strain yields comparable results and is depicted in Figure 1.2.

1.3.2 Stage 2: Dike Formation

1.3.2.1 Dike Opening in Brittle Crust by Magma Ocean Overpressure

Light fluid underlying a dense crust will experience an upwards buoyancy pressure. This pressure is given by

$$P_{ex} = gh\Delta\rho \tag{1.1}$$

where h is the thickness of the crust and $\Delta\rho$ is the density contrast between the crust and the liquid interior. This quantity is likely of order a few percent of ρ and is a combination of contraction due to crystallization, contraction due to cooling, and light element exclusion during crystallization. For an eruption to occur, this excess pressure must exceed compressional stresses in the elastic crust. Assuming the crust is already fractured, the stress to move a lithospheric fault (i.e. the maximum differential stress that can be present in the lithosphere) for the nominal crustal thickness of 10 km is given by Turcotte and Schubert (2014)

$$\sigma_{max} = \frac{2f_s\rho gh}{(1+f_s^2)^{1/2} - f_s} \tag{1.2}$$

$$\approx \frac{\rho}{4}gh \approx 2 \text{ MPa} \tag{1.3}$$

where $f_s \approx 0.65$ is the coefficient of friction on crustal faults. This indicates that the lithosphere is able to support compressional stresses about $\frac{\rho/4}{\Delta\rho} \approx 10$ times larger than the excess hydrostatic pressure produced by its weight on the molten interior. However, contraction can easily exceed this stress and cause faults to fail. With E as Young's Modulus, the strain required is $\frac{\sigma_{max}}{E} \approx \frac{2\times10^6}{10^{11}} = 2\times10^{-5}$, which accumulates in $\frac{2\times10^{-5}}{10^{-15}\ \text{s}^{-1}} \approx 1$ kyr, so faults will frequently move and relieve stress. Assuming that fault motion is able to relieve most of the accumulated stress (Fulton et al. 2013) within a local area, the excess fluid pressure can then force cracks open during such periods.

1.3.2.2 Fracture Initiation in Ductile Crust

We argued above that melt ascent through the brittle section of the crust is possible, locally and temporarily, despite the overall compressional stress environment. However, the

melt needs to be able to first ascend into the brittle region of the crust, which requires propagation through the nominally ductile lower crust. If partial melt is present in this region, porous flow may feed shallower, macroscopic dikes (Rubin 1998). Below we will discuss the initiation of fractures at (or near) the base of the crust in the absence of partial melt, and then their ability to propagate under the influence of inflowing melt.

One problem that has to be overcome to form a fracture is the ductility of the iron near the base of the crust. Near its melting point, solid iron has a viscosity of $\sim 10^{11}\text{Pa} \cdot \text{s}$ (Frost and Ashby 1982) and thus a viscoelastic response (Maxwell) timescale of 1 s, so for it to respond in a brittle fashion, the strain rate has to exceed 1 s^{-1}. The other major difficulty is the fact that iron has a high tensile strength, on the order of 100 MPa (Ashby 1999, Figure 4.4), so large stresses are needed for fractures to form. These factors make fracture propagation much more challenging than the equivalent problem in silicate settings (Jellinek and DePaolo 2003; Karlstrom and Richards 2011, e.g.).

The most likely way to generate large stresses quickly is from cratering. Peak pressures on the order of hundreds of MPa occur to depths of 10 to 100 times the impactor radius, depending on the impact velocity (Melosh 1989, Section 5.2). Thus, for impactors with radii around 1 km, fractures should extend through to the base of the crust while it is still only tens of kilometers thick. The role of impacts in volcanism is observed elsewhere in the solar system, particularly on Mercury where volcano occurrence is strongly associated with craters (Klimczak et al. 2018).

1.3.2.3 Dike Propagation

Once a fracture has formed, it will propagate if the forces trying to extend it exceed the forces resisting that extension. The fluid in the fracture is buoyant, generating stresses which tend to elongate the dike. The stress from buoyancy grows with dike length, so this force becomes more important in longer dikes. Strength in the host material serves to limit growth, because fracturing at the tip of the dike is required for its extension (Rubin 1995). A compressional background stress increases the buoyancy required for a dike to propagate. Crawford and Stevenson (1988) derive an expression for the minimum length a dike must reach before pressure from melt buoyancy can fracture the crust and force the crack to open further.

A dike will propagate itself when

$$K_c = (\pi l_{crit})^{1/2} \left[T + 2g\Delta\rho l_{crit}/\pi\right] \tag{1.4}$$

Here T is the local stress in the crust, defined here to be positive for tensile stress, K_c is the fracture toughness, and l_{crit} is the minimum length for a dike to become self propagating. To propagate itself vertically against 100 kPa of compressive stress (∼5% of what faults can support), a dike would have to be 11 km long. If, on the other hand, there were 200 kPa of extensional stress, this critical length is less than 1 km. At $T = 0$ the expression reduces to the result from Lister and Kerr (1991),

$$l_{crit} = \left(\frac{K_c}{\Delta\rho g}\right)^{2/3} \approx 7 \text{ km} \tag{1.5}$$

Even modest compressional stresses therefore result in critical crack lengths larger than the thickness of the entire crust. We thus conclude that the only time dike propagation is likely to occur is immediately after a faulting event has reduced the local compressional stress to approximately zero.

Dikes will be much more easily able to propagate if there is local tensile stress. There are at least two ways to generate local tensile stress which we expect to be present. One is impact craters. However, although we do not rule these out entirely, craters which are sufficiently large to generate rebound and tensile stresses near the base of the crust are likely to be uncommon. An alternative is for material to delaminate (i.e. detach and descend as a diapir) from the base of the crust, imparting rapidly-changing stresses to the material immediately above. Solid material tends to delaminate from the crust because it is more dense than the melt immediately below it, and at the base of the crust temperatures are high enough, and thus viscosities low enough, for material to flow. Delamination has been discussed on Io (Kirchoff and McKinnon 2009), as well as on metallic asteroids (Neufeld et al. 2019), and in the latter case is expected to recur on timescales of a few tens of kyr. The stress will vary in and around the diapir, but Kirchoff and McKinnon (2009) point out that its magnitude is roughly $\sigma \sim \Delta\rho g\lambda$ where λ is the thickness of the layer being shed.

Based on Neufeld et al. (2019), the diapirs will have a length scale of about 1 km. Thus,

delamination will generate stresses of order 100 kPa. Delamination also has the advantage of being a recurrent phenomenon, so the base of the crust is constantly being stressed and unstressed.

Assuming fluid injection timescales of tens of kyr, the bottom 60% of the crust is expected to be dominated by viscous processes, potentially leading to the growth of larger intrusions than the initial dikes (cf. Karlstrom et al. 2017). Such intrusions, however, would still be buoyant relative to the solid crust, and thus likely to ascend promptly rather than being stored.

1.3.2.4 Dike Refreezing During Ascent

Melt forced upward through a crack will lose heat to crack walls and eventually refreeze. For eruptions to occur, the timescale of freezing needs to be longer than the timescale of melt ascent (e.g. Petford et al. 1994). Given the low viscosity of iron, the flow may be turbulent, in which case for a dike of width D the ascent velocity is given by (Wilson and Head 2017):

$$u = \sqrt{D \frac{g}{f_d} \frac{\Delta\rho}{\rho}} \tag{1.6}$$

where f_d is the coefficient of drag on the crack walls. To refreeze, we need the dike walls to absorb a heat per area of $D\rho L$, where L is the latent heat of freezing. For eruption timescale t and thermal diffusivity κ, this will propagate a distance $\sqrt{\kappa t} = \sqrt{\kappa h/u}$ into the walls, carrying away a heat per area of $C_p \rho \Delta T \sqrt{\kappa t}$, where C_p is the heat capacity of the walls. Setting these equal gives the width of the smallest crack that will refreeze

$$D_{min} = \left(\left(\underbrace{\frac{C_p \Delta T}{L}}_{\sim 10^{-1}} \right)^4 \underbrace{\frac{(\kappa h)^2}{g}}_{\sim 1\,\mathrm{m}^5} \underbrace{f_d}_{\sim 10^{-1}} \underbrace{\frac{\rho}{\Delta\rho}}_{\sim 10^{1.5}} \right)^{1/5} \approx 0.3 \text{ m} \tag{1.7}$$

where here we have taken h=10 km, g=0.1 m s^{-2}. This minimum width is similar to Earth, where basalt has a minimum width of 1 meter (Rubin 1995), so reasonable width cracks are able to avoid refreezing. Assuming a viscosity of 10^{-2} Pa $\cdot$ s, these values give us a Reynolds number greater than 10^3, so using the turbulent velocity is appropriate.

1.3.3 Stage 3: Dike Closing, Reestablishing Compressional Regime

1.3.3.1 Eruption Volume

Eruptions are self-limiting processes, because compressional stress reaccumulates as the liquid volume reduces and the crust subsides. An eruption will stop when the stress in the crust is equal to the excess pressure in the ocean ($gh\Delta\rho$). If, at the beginning of an eruption, the difference between the ocean excess pressure and the local crustal stress is P_{net}, then assuming the interior melt only compresses elastically (i.e. has zero volatile content), a corresponding strain of $\epsilon = \frac{P_{net}}{E}$ will accumulate. Treating the eruption as a layer covering the entire body with thickness δ, then $\epsilon \approx \frac{\delta}{R}$. If we assume that faulting has relieved all compressional stress in the crust, $P_{net} = gh\Delta\rho$ and

$$\delta = \frac{gh\Delta\rho R}{E} = \frac{\frac{4}{3}\pi G h \rho \Delta\rho R^2}{E} \tag{1.8}$$

$$= 0.3 \text{ m} \times \left(\frac{\Delta\rho}{150 \text{ kg/m}^3}\right)\left(\frac{R}{100 \text{ km}}\right)^2\left(\frac{h}{10 \text{ km}}\right)\left(\frac{10^{11} \text{ Pa}}{E}\right) \tag{1.9}$$

If some stress remains in the crust this value will be diminished somewhat. The nominal value of δ implies an eruption volume V_{erupt} of 40 km^3.

Eruptions will advect heat equal to $V_{erupt}\ \rho(C_p\Delta T + L) \approx 10^{20}$ J. With a surface thermal gradient of 0.1 K/m this is roughly 10 years of global conductive heat loss. The importance of advection thus depends on how frequently those eruptions occur relative to this 10 year value.

1.3.3.2 Eruption Interval

After an eruption, compressional crustal stress will be reestablished and the crust will once again need to accumulate $\sigma \approx \frac{\rho g h}{4} \approx \rho^2 h G R$ stress (as discussed in stage 2, above) before this particular fault will fail again. New solid plated onto the base of the crust with thickness Δh, will create a strain

$$\epsilon = \frac{\Delta h}{R}\frac{\Delta\rho}{\rho} \tag{1.10}$$

which can be rearranged to solve for the thickening required to cause the next failure

$$\Delta h = \frac{\frac{\pi}{3}\rho^3 R^2 h G}{\Delta\rho E} \approx 150 \text{ m} \times \left(\frac{150 \text{ kg/m}^3}{\Delta\rho}\right)\left(\frac{R}{100 \text{ km}}\right)^2\left(\frac{h}{10 \text{ km}}\right)\left(\frac{10^{11} \text{ Pa}}{E}\right) \tag{1.11}$$

Using $\Delta t = \frac{2h\Delta h}{\kappa}$ we end up with failure every few kyr. The fact that this is large compared to the 10 years above means that eruptions do not play a significant role in the thermal evolution of the body.

This process differs from volcanic stress accumulation on Earth. On Earth, magma chamber stresses can transition from elastic/brittle- to viscously-accommodated as the thermal environment around the magma chamber changes (Jellinek and DePaolo 2003). In our case, stress arises from global volume changes associated with solidification, and the thermal environment across the crust changes only very slowly: viscous relaxation is always rapid at the base of the crust (Sec 3.2.2), and always negligible at the surface.

Note that in both of the previous sections we treated these processes as if all of the planet's stress accumulation and relief occurs on a single fault, which is certainly not the case. In reality, faulting and erupting depends fundamentally on local stress evolution, so global stress does not directly capture these events. The value of treating eruptions this way is that it captures the relative volumes of erupted and deeply crystallized material, and thus reflects the role of eruptions in the body's overall thermal evolution.

1.3.3.3 Total Erupted Volume

A useful value to look at is the erupted layer thickness, δ, divided by the thickness of plating needed for eruption, Δh,

$$\frac{\delta}{\Delta h} = \frac{\frac{4}{3}\pi G h \rho \Delta\rho R^2/E}{\frac{\pi}{3}\rho^3 R^2 h G/\Delta\rho E} \tag{1.12}$$

$$= \left(2\frac{\Delta\rho}{\rho}\right)^2 \approx 10^{-3} \tag{1.13}$$

Importantly, most of the uncertain parameters that went into δ and Δh cancel (note that the E in the numerator and the denominator only cancel if the liquid and solid have similar elastic moduli, which may not be the case in the presence of volatiles, as discussed below). This means that although erupted volumes and frequencies are very uncertain, the total amount of

material that can be erupted is much better constrained. This value is an upper limit, because it reflects the volume fraction of the body to participate in eruptions if every faulting event relieves all local compressional stress and leads to an eruption. The real value is likely to be smaller. One thousandth of the body as an upper limit on material erupted means that eruptions will not play a major role in thermal and stress evolution, serving only to modify the surface. This is in contrast to, for example, Io, where volcanism is the dominant source of heat transfer (e.g. Moore et al. 2016).

1.4 Role of Volatiles

There are two important ways that volatiles can alter the behavior of iron volcanism. The first is the fact that they will be excluded from the crystallizing solid, making the melt more buoyant than implied by just the phase transition and thermal contraction. Sulfur in particular is likely to be present (Chabot and Haack 2006) and can be expected to play this role, but its concentration is a major unknown. In an extreme case, native sulfur might erupt, in a similar manner to the sulfur volcanism proposed for Io (Sagan 1979; Williams et al. 2001), but eruption of an Fe-S alloy is much more likely. Any light elements present in the melt should serve to enhance volcanism, but how significant a role this plays is difficult to predict.

The second way that volatiles can be important parallels a role they play in silicate magmatism, and likely play in cryovolcanism. As pressure is relieved during eruptions, volatiles may exsolve and form bubbles, lowering the density of the melt column, accelerating its ascent and also increasing its compressibility (Bower and Woods 1997). This process is difficult to predict because it not only requires knowing the initial volatile content of the iron, but also the tendency of those volatiles to exsolve. Further complicating this is the fact that mantle stripping is a violent process (Asphaug et al. 2006) which may have already exposed the bulk of the core to vacuum, removing volatiles which could provide a bubble source. We therefore do not pursue this issue any further here.

1.5 Geomorphic Implications and Potential Constraints from Observation

Identifying iron volcanoes on metallic asteroids may prove to be challenging. Searches for cryovolcanism motivate caution in interpreting features as volcanic in origin: Moore and Pappalardo (2011) provide a summary of several past mistaken identifications of cryovolcanism, an important warning for further searches for volcanoes. In addition, any such volcanoes have had more than 4 billion years to be modified. 16 Psyche, for example, is far from hydrostatic (Shepard et al. 2017), and if not a rubble pile must at least be heavily altered by impacts.

In the event that metallic volcanoes can be identified using present-day observations, they will likely be very informative. For example, it is likely that volcanoes will be spatially associated with impact craters, analogous to what is seen on Mercury (Klimczak et al. 2018), and the degree of this association will inform the stress evolution of the crust. A rapidly-cooling metallic flow may acquire a remanent magnetic field, if an internal dynamo is active at that time (Bryson et al. 2015). Similarly, the style of volcanism on the body alone provides substantial insight. Because there is no analog to the buoyant continental crust on Earth, the development of large mid-crustal magma chambers and calderas is less likely on iron asteroids. If the volcanism is effusive, the structures it builds will constrain erupted volume and viscosity. If the volcanism is explosive, the eruptive behavior will depend on the volatiles present and the reservoir conditions (Bower and Woods 1997; Lu and Kieffer 2009) and will have major implications for light element incorporation in cores, volatile retention during mantle stripping, and devolatilization during subsequent evolution. We caution, however, that in the latter case the eruption velocity could easily exceed the escape velocity ($\approx$200 m/s) making identification of volcanic deposits more challenging than on e.g. Mercury.

1.6 Evidence in the Meteorite Record

A key prediction that follows from metallic volcanism is that bodies hosting it will have two end-member types of solids which experienced very different histories. Material crystallizing onto the bottom of the crust will cool slowly and will exhibit an inverse

correlation between cooling rate and light element content. Erupted material will crystallize very quickly, and unless it is reheated will show ∼instantaneous cooling. This quenching will prevent elemental fractionation, so erupted material will record the (non-volatile) element abundances of the liquid interior at the time it was erupted. Incompatible element (Ga, Ge, Ir, etc.) concentrations will be much larger than contemporaneously formed deep solids. These meteorites would likely be some of the most incompatible element enriched material in their meteorite family. If volatile exsolution is involved, the quenched solids would likely contain vesicles. However, because erupted material is a small volume fraction of the body, the quenched meteorites will likely be rare. Although a detailed analysis is beyond the scope of this paper, it is plausible that the modern meteorite record can serve as a test of this paper's predictions.

It is important to note that there are two important differences between how silicate and iron cooling and crystallization are recorded in hand specimens. First, the texture of iron specimens is controlled by sub-solidus processes (Wasson 1985; Hutchison 2004), so no textural evidence of how crystallization occurred is retained. Sub-solidus textures can, however, be used to determine cooling rates (Sec 1). Second, chemical evidence of the crystallization process (e.g. dendrites) may be retained, but is predicted to vary on length-scales much larger than available iron meteorite specimens (Haack and Scott 2009), so no spatial information on this process is available.

1.7 Conclusions

We predict that many metallic asteroids will have hosted volcanic activity while solidifying. Overall, metallic volcanism should bear more resemblance to silicate volcanism than cryovolcanism. This is because, like silicates, the melt is buoyant, and the thermal conditions under which melt travels through dikes are similar. However, fracture initiation is more difficult in metallic systems because of the ductility and tensile strength of iron, while fracture growth is opposed by the large fracture toughness of iron and the background compressional environment. Nonetheless, we predict that metallic volcanism is possible in areas where cratering has generated fractures and the local stress has been reduced by faulting.

The details of the hypothesized processes will require substantial further theoretical

investigation. Geomorphological examples of iron volcanoes would make for particularly striking confirmation, but will likely be very difficult, if not impossible, to unambiguously identify. More likely, testing of this hypothesis will come from the meteorite record, either by explaining existing anomalies in the record or predicting the characteristics of future meteorites.

Table 1.1: Parameters Used

	Description	Value	Source
κ_s	Silicate thermal diffusivity	1.1×10^{-6} m^2/s	(Carslaw and Jaeger 1959)
κ_m	Metal thermal diffusivity	1.2×10^{-5} m^2/s	(Carslaw and Jaeger 1959)
T_m	Melting point	1200 K	Assumed
T_s	Temp. due to solar irradiation	200 K	Assumed
L	Latent heat	2.7×10^5 J/kg	(Haack et al. 1990)
C_p	Specific heat capacity	569 J/kg·K	(Carslaw and Jaeger 1959)
Q	Activity energy	2.5×10^5 J/mol	(Frost and Ashby 1982)
R_g	Gas constant	8.314 J/mol·K	
R	Body Radius	100 km	Assumed
g	Acceleration due to gravity	[m/s^2]	
ρ	Density	7400 km/m^3	(Carslaw and Jaeger 1959)
$\Delta\rho$	Density contrast, melt vs solid	$\approx \rho/40$	Assumed, very approximate
h	Crust thickness	[m]	
h_e	Brittle crustal layer thickness	$h/2$	Calculated, approximate
P	Pressure	[Pa]	
f_s	Coefficient of friction on faults	0.65	(Turcotte and Schubert 2014)
f	Drag coefficient in dikes	0.1	Assumed
σ	Stress	[Pa]	
ϵ	Strain	dimensionless	
$\dot{\epsilon}$	Strain Rate	[s^{-1}]	
K	Bulk Modulus	10^{11} Pa	(Ahrens and Johnson 1995)
K_c	Fracture Toughness	10^7 Pa·m$^{1/2}$	(Ashby 1999, Figure 4.7)
D	Dike width	[m]	
Δh	Crystallized layer thickness	[m]	
δ	Erupted layer thickness if global	[m]	
l_{crit}	Dike Critical Length	[m]	(Crawford and Stevenson 1988)
λ	Diapir Thickness	[m]	

Note that entries without values or without sources are outputs we are finding. Brackets indicate units when a specific value is not relevant.

Chapter 2

Improved determination of Europa's long-wavelength topography using stellar occultations

This chapter is a slightly modified reprint of work previously published as:
Jacob N.H. Abrahams et al. (2021). "Improved Determination of Europa's Long-Wavelength Topography Using Stellar Occultations". In: *Earth and Space Science* 8.7. DOI: 10.1029/2020EA001586.

Abstract

Europa Clipper will arrive at Jupiter at the end of this decade and will explore Europa through a series of flybys. One of its many goals is to characterize Europa's topography and global shape using the EIS and REASON instruments. In addition, Europa Clipper's UV Spectrograph will observe stars pass behind (be occulted by) Europa. The spectrograph has sufficiently precise timing, corresponding to a topographic precision of order meters, that these occultations can also serve as altimetric measurements. Because of gaps in the REASON radar altimeter coverage imposed by the flyby geometries, the

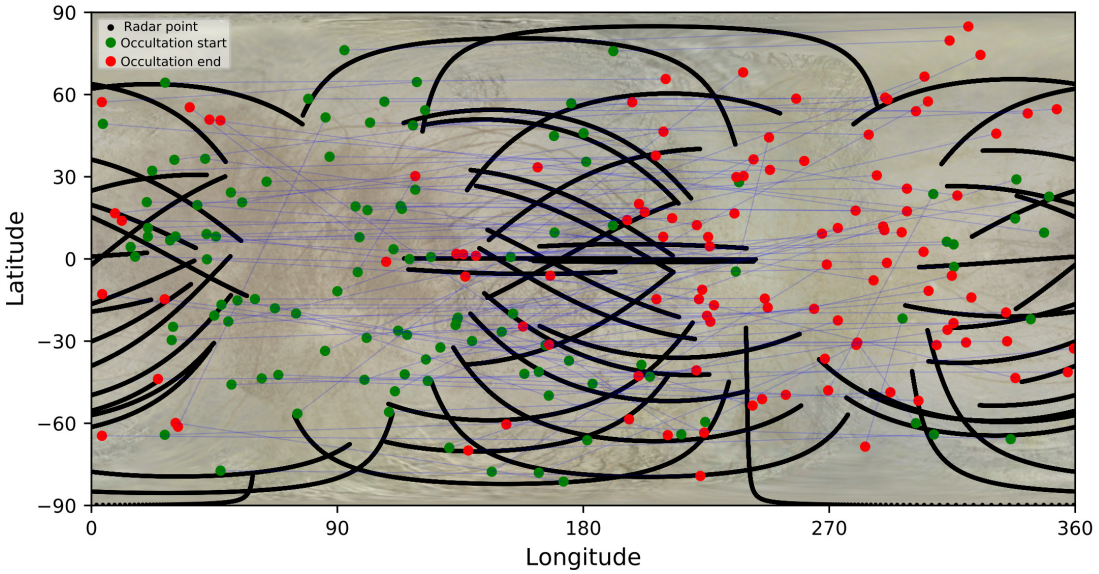

Figure 2.1: Map of radar altimetry profiles at altitudes <500 km (densely spaced black dots) and likely occultation opportunities (green for ingress and red for egress, individual chords connected by a blue line) for trajectory 19F22. Notably, the radar measurements are concentrated around the subjovian and antijovian points. This results in global shape fits with large misfits at wavelengths smaller than the size of the gaps. The occultation measurements are able to fill in some of these gaps, significantly improving global coverage. Note that this map is based on proposed trajectories that are still evolving, but the general trend of altimetry profiles being concentrated at the sub- and anti-jovian points and occultations being more uniformly distributed comes from inherent orbital constraints. There are 109 total occultations and 283571 radar measurements across 46 separate tracks. Background map created by Björn Jónsson.

addition of ∼100 occultations results in a substantial improvement in the recovery of Europa's long-wavelength shape. Typically five extra spherical harmonic degrees of topography can be recovered by combining occultations with radar altimetry.

2.1 Introduction

Europa's global shape is only poorly constrained, with our best models inferred from four Galileo limb profiles (Nimmo et al. 2007). Obtaining more precise global and regional topography is important if we want to understand Europa's internal structure and the state of its ice shell (Hemingway et al. 2013; Ojakangas and Stevenson 1989), and is an objective of the Europa Clipper mission (Pappalardo et al. 2019). The primary instruments for determining Europa's global shape are the radar instrument REASON (Radar for Europa Assessment and

Sounding: Ocean to Near-surface) (Blankenship et al. 2018) and the visible imager EIS (Europa Imaging System) (Turtle et al. 2019). The main limitation in fitting global shape is the fact that neither the radar tracks (black dots in Figure 2.1) nor the EIS limb profiles have complete global coverage, instead having gaps around the poles and longitudes near 90° and 270° as a consequence of Europa Clipper's resonant flyby geometry. Filling in those gaps has the potential to dramatically improve our ability to fit the global shape and its time variation. A similar problem was encountered by the MESSENGER mission to Mercury, and a similar solution was employed: sparse radio occultation measurements of southern hemisphere topography were used to augment dense altimetric measurements of the northern hemisphere (Perry et al. 2015).

In this paper we focus on combining occultations with REASON altimetry to demonstrate the utility of stellar occultations for filling in data gaps and improving our knowledge of Europa's shape. In reality, EIS limb profiles will also contribute, despite suffering from similar gaps to REASON; to keep our analysis simple, and to explore the important role of the radar altimetric cutoff, we do not consider their contributions further below.

Europa Clipper's UV Spectrograph (UVS) (Retherford et al. 2015) will observe stars as they pass behind Europa, with the primary goals of studying potential plumes and a tenuous atmosphere. Notably, however, the instrument's maximum temporal resolution is ∼1 millisecond. Because the apparent velocity of stars relative to Europa is of order 1 km/s, the timing of an occultation is equivalent to a measurement, with an uncertainty on the order of meters, of the relative positions (in the direction of travel) of Europa, Europa Clipper, and the star. If the spacecraft and star positions are well known, this is equivalent to a ∼1 m resolution measurement of the position of Europa's surface. Alternatively, if the star's disappearance and reappearance are both observed, then the spacecraft and star position uncertainty mostly cancel out and the duration of the occultation is equivalent to a ∼1 m resolution measurement of a chord across Europa. In this paper we focus on two-sided occultations, chords, which allow us to ignore uncertainties in spacecraft tracking and stellar catalogues. In reality, many occultations will likely be one-sided; in this case, the analysis would proceed in a similar fashion to that described below, but the effect of these extra uncertainties would need to be considered.

Stellar occultations have the significant benefit of being well distributed across the satellite,

meaning they fill in a lot of the radar profiles' gaps, as shown in Figure 2.1. Although the actual spacecraft tour will differ from those used in this figure, the spatial distribution of the two data sets will remain qualitatively the same. As mentioned above, in this paper we only consider chords, where we know the time of the star's disappearance and reappearance.

Ice shell structure, and therefore global shape, is a high priority target for Europa Clipper because it is key to understanding several fundamental features of a planetary body. For example, Ojakangas and Stevenson (1989) predicted long-wavelength variations in ice shell thickness (and thus topography) on Europa, caused by spatial variation in tidal heating. This was then investigated by Nimmo et al. (2007) who were able to place upper limits on the amplitude of shell thickness variations using Galileo data. Measurements by Europa Clipper will further refine those constraints, and may be able to detect any nonzero shell thickness variations. A positive detection of the predicted long-wavelength variations would help constrain Europa's shell thickness and rate of heating. If no such variations are detected, then either the shell must be very thin or the base of the shell must have such a low viscosity that it can erase variations as they form.

Measurements of a body's long wavelength shape, typically expressed in terms of spherical harmonic coefficients of degree l and order m, are useful for at least two additional reasons. First, the topographic roughness spectrum of a body may itself contain information about geophysical parameters of interest, such as elastic thickness (Araki et al. 2009; Nimmo et al. 2011), interior rheology (Fu et al. 2017), and surface structure (Ermakov et al. 2019). Second, the ratio of a body's gravity to topography at different values of l - the admittance - captures key information about its structure, and has been employed very successfully around the solar system. For example, admittance has been used to infer the rigidity and weathering of Titan's ice shell (Hemingway et al. 2013), the thicknesses and densities of the crusts of Mercury (Sori 2018) and Enceladus (Iess et al. 2014; Hemingway and Mittal 2019), and the compensation state and subsurface rheology on Ceres (Ermakov et al. 2017; Ruesch et al. 2019).

Finally, measuring Europa's diurnal tidal deformation would be helpful in understanding ice shell thickness and rheology (Moore and Schubert 2000; Wahr et al. 2006; Steinbrügge et al. 2018), and the high precision of occultations suggests they could be helpful in identifying tides. Surface deformation is particularly valuable to measure because it yields one Love number, h_2. When h_2 is combined with a second Love number, k_2 (derived from gravity

moments), it becomes possible to obtain a substantially better estimate of the shell thickness than is possible with either measurement alone. Wahr et al. (2006) lay out this process in detail for Europa. REASON will seek to constrain Europa's tides by looking for time-dependence at the points where radar tracks intersect (Steinbrügge et al. 2018). It would be very valuable if UVS occultations can also help constrain Europa's tides, so we conducted a preliminary search for tides, but as discussed later we find that our expected ∼hundreds of stellar occultations are not sufficient alone to fit tides.

The primary challenge for studying Europa's global shape with radar altimetry is the fact that Europa Clipper will orbit Jupiter and only study Europa during flybys. This means that the measurements it is able to make are limited by orbital dynamics . In particular, Europa Clipper's closest approaches are clustered around Europa's subjovian and antijovian points, resulting in coverage gaps at the centers of the leading and trailing hemispheres, and towards the poles (Figure 2.1). As we describe later in this paper, gaps of this nature greatly restrict our ability to determine spherical harmonic coefficients. A good rule of thumb is that a gap of X degrees results in a maximum possible recovered degree of $l_{max} \approx 360°/X$. The great advantage of occultation profiles is that they fill in these gaps and thus allow topography to be recovered to higher degrees. The number of available UVS occultation events increases with proximity to Europa, but in principle the occultation measurement works equally well at infinite distance, enabling much more uniform global coverage.

In this paper we explore how combining UV Spectrograph occultations with radar altimetry can improve global shape fits. We demonstrate that adding occultations increases the maximum degree that can be fit and decreases the typical misfit in general.

2.2 Methods

To explore whether occultation data can help characterize Europa we 1) take an assumed shape model (Section 2.3.1.4), 2) generate synthetic radar and occultation data from it, and then 3) explore our ability to retrieve our original shape model using those synthetic data. In order to identify what is important for shape fitting, we fit a shape model in three different ways: using only radar data, only occultation data, and both datasets combined (Figure 2.2). In addition, we explore adding tides to our data (Section 2.3.2), and what happens when we

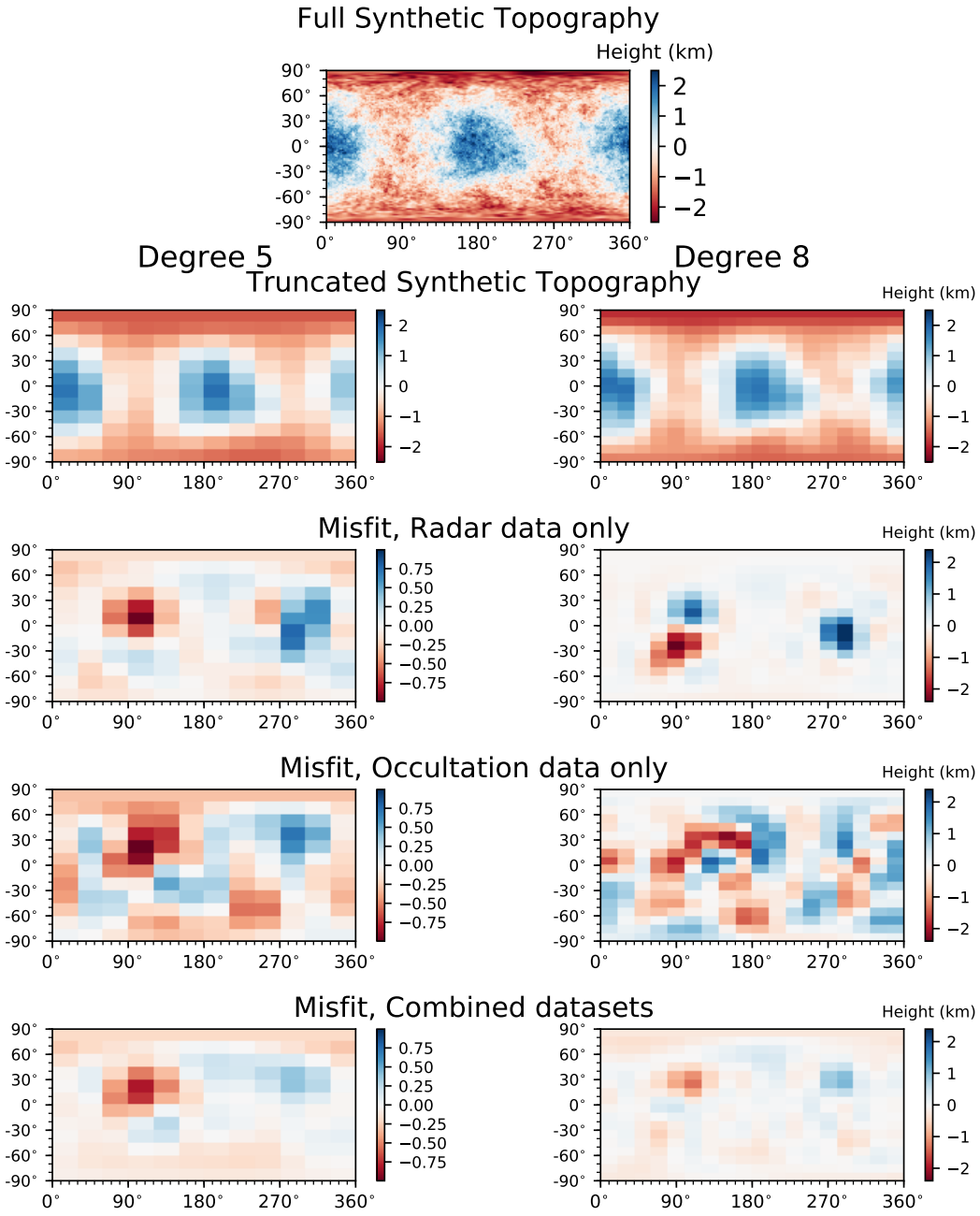

Figure 2.2: Illustration of fits at two different degrees. The top panel shows the map with which we generate our synthetic data. The first row shows that same map, but truncated at spherical harmonic degrees 5 and 8. Then the next three rows are misfit maps for fits using only radar data, only UVS chords, and with both datasets simultaneously. For each of those fits, we prescribe a degree out to which we want to fit (5 or 8 for this plot) and then attempt to fit all degrees and orders up to that degree. Note that the left and right column misfit maps have different color scales and the degree 8 fits all have ∼2-3 times larger errors than their degree 5 counterparts.

modify our shape model, our measurement locations, and our measurement precision (Section 2.3.1). We assume that when they are usable (Section 2.3.1.3) radar data are perfectly precise, and we generally make the same assumption for occultation chords – see Section 2.3.1.2 for discussion and testing of these assumptions.

We use least-squares to find the set of spherical harmonics that best fit our synthetic data, in a similar fashion to Nimmo et al. (2011). Generically, this involves solving the matrix equation

$$\hat{\boldsymbol{x}} = \left(\underline{\boldsymbol{A}}^T \cdot \underline{\boldsymbol{A}}\right)^{-1} \cdot \underline{\boldsymbol{A}}^T \cdot \boldsymbol{z} \tag{2.1}$$

where $\hat{\boldsymbol{x}}$ is the vector of coefficients that we want to fit and $\boldsymbol{z}$ is a vector of measurements. For our work, $\hat{\boldsymbol{x}} = \{C_{00}, C_{10}, C_{11}, S_{11}, \cdots, C_{NN}, S_{NN}\}$, the spherical harmonics we want to fit, and $\boldsymbol{z} = \{c_1, c_2, c_3, \cdots, c_M\}$, the set of measured occultation chord lengths. The elements of the matrix $\underline{\boldsymbol{A}}$ are defined by $A_{ij} = \frac{\partial z_i}{\partial x_j}$. Further details for computing $\underline{\boldsymbol{A}}$ and our spherical harmonic conventions are in Appendix A. Each term in the matrix $\underline{\boldsymbol{A}}$ can be well approximated analytically, and we solve Equation 2.1 numerically.

If the topographic power spectrum is known a priori, an additional damping term can be added to Equation 2.1 to avoid large oscillations in areas with no data coverage (Nimmo et al. 2011). We did not apply such a term here because we are interested in how well we can recover topography without imposing additional assumptions.

We can also, optionally, include an extra term in $\hat{\boldsymbol{x}}$ corresponding to tidal amplitude, and attempt to fit Europa's time-varying shape as it deforms over its orbit, as discussed further in Section 2.3.2.

Because we do not yet know Europa's real shape precisely enough, this paper fits synthetic data intended to approximate what Europa Clipper will encounter. We assume Europa's shape, calculate what the radar and occultation measurements would be for that assumed shape, and then run our fitting script on those synthetic measurements. The primary shape we assume is designed to match the power spectrum in the global fits in Nimmo et al. (2007). Our nominal shape model is discussed more in Section 2.3.1.4 and is shown in the first panel of Figure 2.2.

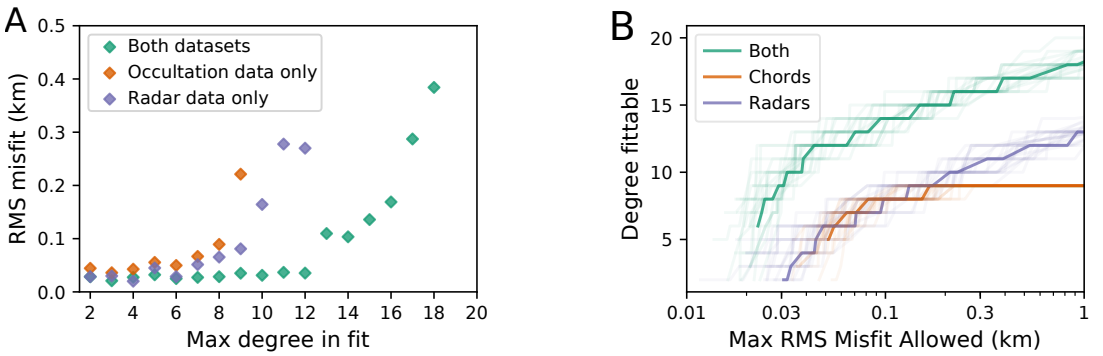

Figure 2.3: A) Average misfit as a function of the total degree we attempt to fit for our nominal shape model. Combining UVS chords with radar data marginally improves fits in general, and significantly extends the total degree that can be well fit. In panel B) we assume there is some cutoff misfit considered "acceptable", and as a function of that cutoff we show the maximum spherical harmonic degree that the individual and combined datasets are able to achieve. We run a suite of fits, varying our shape models according to Section 2.3.1.4, and plot each individual run as a faint line. The ensemble average is plotted with the solid lines.

2.3 Results

Figure 2.2 illustrates our nominal shape model, as well as that shape model truncated at two different spherical harmonic degrees and our attempts to fit those truncated shape models. Broadly, we are able to fit low degrees and our fits degrade at higher degrees. As expected, the errors in the radar-derived shape model are largest around the leading and trailing hemispheres, where there are no observations. Combining radar with occultation data decreases the misfit in general, because we are using more data. More importantly though, it increases the maximum spherical harmonic degree that can be fit at all because the occultation chords fill in the radar altimetry gaps.

Figure 2.3 shows that combining occultation data with radar data allows significantly better fits than either dataset alone. In particular, Figure 2.3a shows the radar-derived topography breaks down above $l = 9$, which is consistent with the existence of gaps approximately 45° wide in the radar coverage (Figure 2.1). The addition of occultation points filling in these gaps allows the topography to be recovered up to $l = 12$. Similarly, Figure 2.3b shows a consistent improvement of roughly 5 extra spherical harmonic degrees when occultations are added to the radar data. Finally, Table 2.1 lists the uncertainties in some recovered low-order spherical harmonics, again showing the improvement obtained by adding in the occultation points.

	C_{20}	C_{22}	C_{40}	C_{44}
Actual (m)	-581	594	-43	42
Radar only uncertainty (m)	35	36	42	30
Chord only uncertainty (m)	45	87	25	53
Combined uncertainty (m)	18	26	22	21

Table 2.1: Precision for our fits for important spherical harmonic coefficients. "Actual" refers to the injected spherical harmonic amplitude. Uncertainties are determined by finding the RMS misfit for individual coefficients over a suite of model runs in which we randomly perturb the input shape model and then fit up to degree and order 5.

2.3.1 Sensitivity to Inputs

2.3.1.1 Number of Occultations

The number of stellar occultations that UVS can observe is highly dependent on tour geometry and data downlink allocation, so it is likely that we receive a different number (possibly a very different number) of occultations than the 109 in our assumed mission plan (trajectory "19F22"). We find that in general, fit quality scales approximately with the square root of the number of occultations. For fits using only chords, the maximum degree that can be fit also scales with the square root of the number of chords, but that effect is more minor for combined (occultation and radar) fits. Overall, more chords unsurprisingly makes for better fits, but while many tours have roughly 200 (rather than the baseline 100) occultation opportunities, it is unlikely that we will collect enough chords to dramatically change the conclusions of this paper.

2.3.1.2 Precision of Measurements

For the bulk of this work, we assumed that measurements were perfectly precise. The motivation for this assumption is that for global fits, we expect our misfit to arise primarily from gaps in global coverage, rather than poor data quality where we have data. That said, it is of course true that at some point, measurement uncertainty will become important. To determine the level where measurement precision becomes the dominant source of error, we inject noise into our data.

Figure 2.4 shows the impact of varying the UVS measurement precision. Notably, fit quality only really begins to degrade when the uncertainty reaches 300 m, and shifts significantly with an uncertainty of about 1 km. The main source of uncertainty in the length

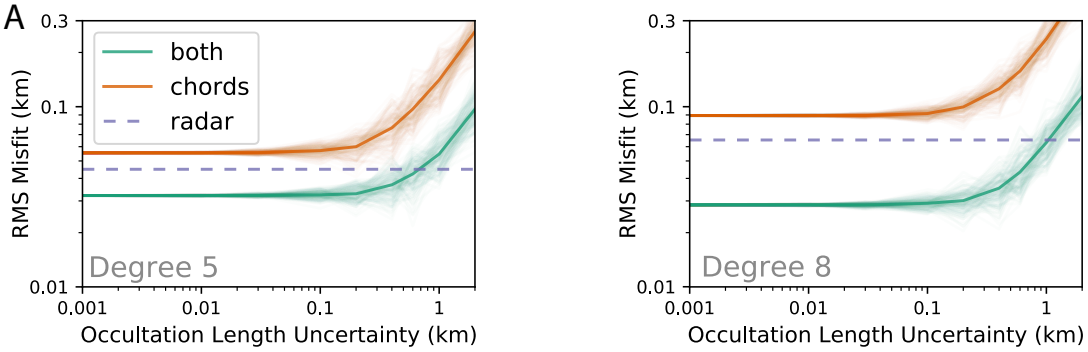

Figure 2.4: The effect of measurement precision on retrievals. We inject random noise into the length of each occultation, and then observe the misfit. Panel **a** is trying to fit shape up to degree/order 5, and panel **b** is trying to fit shape up to degree/order 8. Each faint line is an individual set of chords with varying amounts of noise added, and the dark lines are the ensemble average. We do not inject noise into the radar data; perfectly precise radar retrievals are indicated by the dotted lines for comparison.

of a chord is how precisely timed the stellar ingress and egress are. UVS can collect data at a cadence of up to 1 ms in its pixel-list mode or up to 10 ms in its histogram mode (Retherford et al. 2015). If the spacecraft is moving at 10 km/s relative to Europa, even the 10 ms cadence is only an uncertainty of 100 m. If, instead of collecting chords, observations are only made on one side of an occultation, then the spacecraft position, spacecraft pointing, and stellar position can be significant sources of error, and uncertainties in those quantities would need to be under ∼1 km for UVS occultations to be useful topographic constraints. Overall, occultation timing precision is not expected to degrade global shape fits for two-sided occultations. For one-sided occultations further analysis would be needed, because of the potential role of spacecraft and satellite position uncertainties.

2.3.1.3 Altitude Cutoff for Radar

One of the biggest uncertainties in this work is the range to which useful radar altimetric returns will be obtained, and thus the total length of each altimetry profile. Over the course of a single flyby, Europa Clipper's distance from Europa varies significantly. It is not yet clear within what distance REASON will be able to get a reliable surface return from Europa, because that altitude cutoff depends on the characteristics of Europa's surface, but the baseline for the instrument is 1000 km (pink in figure 5). Steinbrügge et al. (2018) discuss REASON's performance in detail, but, broadly, the effective altimetric range is determined by

a combination of the signal-to-noise ratio of the instrument, and the fact that when using the radar instrument as an altimeter, the "surface" that the radar detects is not necessarily the sub-spacecraft point. Instead, it is the nearest region on Europa's surface which is locally flat and oriented properly with respect to the spacecraft. For example, a mountain near (but not on) the spacecraft trajectory can plausibly be closer to the spacecraft than the surface directly below the spacecraft, and depending on the orientation of its flanks it may produce a misleading return. Further uncertainties arise from the ionosphere of Europa which delays the radio signal (Grima et al. 2015) leading to systematic errors unless corrected by using both frequencies available to the REASON instrument (Scanlan et al. 2019). As a result, the exact performance of radar altimetry depends on uncertain characteristics of Europa and cannot be fully known until arrival. We incorporate these limitations, in a simplified form, by assuming that there is some distance inside of which REASON becomes a reliable altimeter.

For the nominal plots in this work, we assume an altitude cutoff of 500 km. This is an arbitrary choice, and different from REASON's baseline of 1000 km. We chose 500 km primarily because that is the altitude where radar altimetry and occultation chords have roughly the same performance for fitting global shape, allowing the improvements from combining datasets to be most easily seen. Figure 2.5 illustrates what happens when we vary this assumption. In general, the higher the radar altitude cutoff, the better the fits. However, although radar data alone perform better when they extend to higher altitudes, we observe that adding the occultation chords always helps. Thus, although it is hard to accurately predict Europa Clipper's ability to fit global shape using radar alone, it is clear that regardless of the radar performance, occultation chords should always improve those fits.

2.3.1.4 Shape Model Used

To explore the value of occultation chords, we need simulated data to fit, which requires a shape model to generate those data. Without a good current model of Europa's global shape, we needed to assume one. Our nominal topographic model consists of three components. The first is the degree-two shape arising from tidal and rotational distortion alone. The second is topography arising from shell thickness variations due to tidal heating, resulting in power at both l=2 and l=4. These two components are the same as the nominal model in Table 3 of Nimmo et al. (2007). The final component consists of randomly-generated topography up to

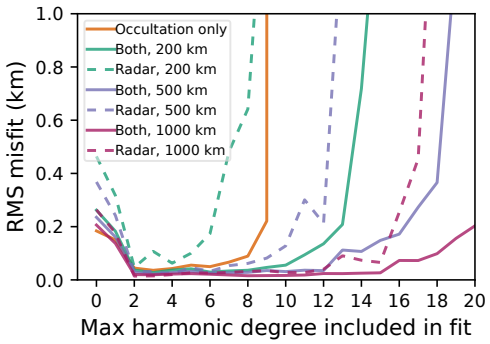

Figure 2.5: Varying the altitude at which the radar data are cut off, showing the evolution of misfit as a function of the degree included in the fit for radar data collected below 200 km, 500 km, and 1000 km. The 1000 km data have roughly twice as many total data points, and the 200 km data have roughly half as many. Radar alone fits the shape better if higher altitude data are included, but regardless of the cutoff, UVS chords always improve the radar fits. One noteworthy feature is the fact that the fits at degrees 0 and 1 are quite bad, and they improve significantly at degree 2, demonstrating the significance of Europa's permanent tidal bulge.

l=180 ($\approx$ 50 km wavelength) and assuming a power-law slope of -1, based on Europa limb profiles (Nimmo et al. 2011). Our model does not include short-wavelength roughness because, as shown in Figure 2.4, topography with an amplitude less than about 100 m does not impact our fit quality.

One potential problem with occultations, as with limb profiles, is that they record the highest point in the line of sight, which may not be at the expected location (on the limb) Perry et al. 2015, e.g. A synthetic analysis by Nimmo et al. (2010) showed that for the icy satellite Rhea this effect did not bias the recovery of long-wavelength topography appreciably. Since Europa is much smoother than Rhea, we expect the same result to hold here.

To ensure we are not just fitting pathologies in one particular model, we test a few different modifications. First, we take our nominal power spectrum, and randomly generate spherical harmonic coefficients that match it, and run our model on a suite of these randomly generated Europas. In addition, we take those power spectra and increase or decrease their amplitudes (preserving their slopes) beyond degree 3, in order to explore whether more or less topography impacts our fits. Finally, we ran our model on a global map of Earth's Moon, rescaled to match Europa's radius and tidal bulge. Our results across all of these modifications were broadly similar, so we consider our results robust to variations in the specific shape model chosen.

2.3.2 Diurnal Tide Fits

Europa Clipper's ability to fit Europa's diurnal tides, and the potential for stellar occultations to improve those fits, is a very important question but requires detailed radar models that lie outside the scope of this paper. We restrict our analysis to whether occultation data alone can detect tides, and find the answer is most likely no. To do this, we inject a time varying signal into the degree 2 harmonics in our shape model and propagate it into our synthetic data, and we modify the vector we are trying to fit ($\hat{\boldsymbol{x}}$ in Section 2.2) so that in addition to a set of spherical harmonics, it contains a parameter for the tidal amplitude. Then we can compare our best fit tidal amplitude to our injected tidal amplitude and assign a misfit. Figure 2.6 shows the distribution of those misfits. Europa's diurnal tidal deformation is expected to have an amplitude of 30 m (Moore and Schubert 2000), and our tidal retrieval misfits are normally distributed with a standard deviation of roughly 60 m, so we cannot reliably detect tidal deformation and we certainly cannot precisely constrain its amplitude. The main reason for this is that no two occultations are likely to occur at the same location (unlike radar data, which can specifically look at the intersections of radar tracks), so there is a degeneracy between local topography and global deformation. We find our tidal misfit decreases with the square root of the number of occultations and with the square root of the amplitude of Europa's topographic power spectrum. Thus, if we get many more chords than we expect, or if Europa has much less topography than expected, occultations have the potential to detect tides (though this would probably take on the order of 1000 occultations, and a meaningful constraint on their amplitude would take significantly more). Occultations alone probably cannot significantly constrain Europa's tidal deformation.

Ultimately, the important question is not whether occultation data can constrain tides, but whether all of Europa Clipper's altimetry can combine to constrain tides. However, unlike previous topics in this paper, our simple model of the radar data as perfectly precise measurements is inadequate. For the bulk of this work, we have taken the conservative assumption of perfectly accurate radar data and demonstrated that, even in this case, occultation chords can still improve the global shape recovery. However, detecting diurnal tidal deformation with perfect radar data is not difficult – the reason tides are likely to be difficult to detect is that the uncertainty in the radar altimetry is significantly more complicated than

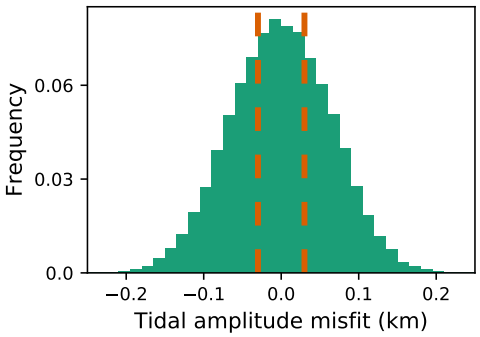

Figure 2.6: Injecting diurnal tidal deformation into the synthetic occultation data, and trying to retrieve its amplitude. Histogram shows the misfit in tidal retrievals, and the red dotted lines show the expected real amplitude of Europa's tides. This distribution is independent of the injected tidal amplitude across a range of amplitudes from one meter to tens of kilometers. These results indicate that UVS occultations alone are not sufficient to reliably detect Europa's tides. Note that "frequency" refers to the fraction of the trials in each bin, it does not integrate to 1.

just instrument noise (Steinbrügge et al. 2018). This means that testing whether occultation data can help radar data to detect tidal deformation requires a much more complete radar model that captures the *limitations* of the radar data, as well as a recreation of the treatment of "cross-over" data that the REASON teams plans. We recommend that future work explore whether occultation and radar data combined allow higher quality tide retrievals, but do not pursue that goal here.

2.4 Discussion and Conclusions

The goal of this work is to highlight the value of stellar occultations for global shape fits, in order to inform future trajectory selection, data volume prioritization, and ultimately to help improve the quality of Europa Clipper mission products. Because these are measurements that were already planned for other purposes, this work shows that we can improve Clipper's ability to constrain Europa's ice shell without any modifications to the mission architecture. The primary value of occultations is the fact that they are fairly uniformly distributed across Europa. This means they have little value for studying local topography, but are perfectly suited for constraining Europa's long-wavelength global shape.

An additional tool to constrain Europa's shape, which has not been included in this analysis, is the Europa Imaging System (EIS) instrument (Turtle et al. 2019) which will image,

among other things, the limb of Europa in order to produce topographic profiles. These limb profiles have the advantage of being linear profiles, rather than point measurements like occultations, and suffer somewhat less from gaps than do the radar profiles. However, the precision of each limb measurement, conservatively 0.2 pixels, is worse by more than an order of magnitude compared to the occultation precision. In any event, limb profiles have the potential to provide further geographically disjoint data, and further improvements to the long-wavelength shape of Europa.

We find that stellar occultations from UVS are very valuable for fitting Europa's global shape. Future work can further refine our understanding of the value of these chords and how best to use them to understand topography. For a very wide range of radar performances, stellar occultations improve the quality of long-wavelength fits, provide an independent check on data collected by other instruments, and improve the spatial resolution that global fits will be able to achieve.

Chapter 3

A theoretical investigation of non-synchronous rotation on Io

This chapter is a slightly modified reprint of work currently in review as: Jacob N H Abrahams et al. (2022). "A theoretical investigation of non-synchronous rotation on Io". In: *In Review*.

Abstract

We investigate the potential for Io to be rotating slightly nonsynchronously. This is motivated by 1) observations that Io's volcanism appears to be offset from where heat is likely being generated, plausibly caused by nonsynchronous rotation on million year timescales, and 2) the fact that Io is strongly heated and will likely behave more like a fluid body than most solar system objects. We combine analytical tidal torque calculations with a mix of analytical and numerical tidal dissipation models to explore the range of plausible rotation rates for Io. We find that the primary control on Io's rotation rate is the strength of its lithosphere, and we expect that its lithosphere is strong. If the lithosphere is weak, the nonsynchronous rotation rate will depend on the interior temperature and periods in the range of Myr to 100s Myr are very plausible. If, as expected, the lithosphere is strong, Io will not rotate nonsynchronously.

3.1 Introduction

By far the most volcanic body in the solar system, Io offers unique insights into tides, volcanism, and the behavior of young silicate planets (Kleer et al. 2019). Unlike planets, whose thermal state and angular momentum budgets are mostly independent of each other, Io's current behavior is controlled entirely by its current and recent relationship to Jupiter. Io's rotation rate is determined by tidal torques from Jupiter, and its thermal budget is set by those same tides (with the energy ultimately supplied by Jupiter's rotation via the Laplace resonance). This link means that a measurement of either Io's rotation or its volcanism is a probe into the other, and both can provide information about Io's interior.

Tidal heating is a result of tides periodically straining a body and the change in that strain producing heat. Because tidal strains are not uniformly distributed across a body, tidal heating will tend to produce heat in particular spatial patterns (Beuthe 2013). Observations of Io's volcanism suggest that Io's volcanic centers do not align with where tidal heat is expected to be produced. Instead, they appear to be offset from predicted patterns of heat production by a few tens of degrees (Hamilton et al. 2013). Suggested explanations for this observation include non-synchronous rotation, tidal heating in a subsurface magma ocean, or variations in the local stress state controlling magma ascent (Hamilton et al. 2013; Kirchoff et al. 2011), but thus far it is difficult to confirm any of them. In this paper, we explore whether nonsynchronous rotation on Io is plausible on a similar timescale to volcano building, and thus could be the cause of the offset in volcanism.

In this scenario, heat would be produced by tides in some longitudinal pattern, and the resulting magma rotated (relative to the tidal axis) away from that pattern. Because volcanoes integrate magma production over time, this would result in volcanism centered away from where heat is being produced at present. The exact location would depend on the volcano formation rate, meaning different styles of volcanism may be offset differently. If it is the case that Io's volcanism pattern is offset by nonsynchronous rotation (NSR), the volcanism serves as a measurement of Io's NSR rate. This in turn tells us about Io's interior structure and rheology, because they determine the nonsynchronous rotation rate.

Torques from a central body on a satellite will tend to drive it toward a spin-orbit resonance, where the orbiting body's rotation period is at or near a rational multiple of its

orbital period (Murray and Dermott 1999). That rational multiple is usually one (with the notable exception of Mercury) which is referred to as "synchronous" rotation. So far, all observations of rotation rates of major satellites conform to this expectation.

However, if the orbiting body is not perfectly rigid and is on an eccentric orbit, the body's rotation rate should be close to, but slightly faster than, synchronous (Greenberg and Weidenschilling 1984). Qualitatively, this could be caused by a combination of two factors. First, an eccentric orbit means that tidal torques vary in strength over an orbit (strongest at closest approach) and that orbital velocity changes over the course of an orbit (fastest at closest approach). This means that the average torque on an eccentric orbit is biased toward the faster part of the orbit, resulting in rotation faster than synchronous. Second, tidal torques only act on a body's non-spherical shape. In a rigid body, that non-spherical shape can be topography or a frozen-in tidal bulge, and will rotate with the body as a whole. In the case of a fluid body, that nonspherical shape is constantly being excited by tides, so its orientation is partially independent of the satellite's bulk rotation. One way to think about the potential for nonsynchronous rotation in a solid body is that it is the body's frozen-in tidal bulge that tides grab onto in order to maintain synchronicity, and as a result, that torque is stressing specifically the frozen-in shape. If that tidal bulge is not perfectly rigid, on long enough timescales the sustained stress will cause the tidal bulge to slowly deform, which will appear as the satellite slowly rotating under that bulge (see e.g. Leconte 2018; Correia et al. 2014).

Because Io is so strongly tidally heated, its interior is likely more fluid than many satellites (if not outright molten (Khurana et al. 2011)). This makes it a particularly strong candidate for observing nonsynchronous rotation. So far, searches for nonsynchronous rotation of Io have not observed any, and have ruled out nonsynchronous rotation periods shorter than a few kyr (Hoppa et al. 1999). We are interested in nonsynchronous rotation on volcano-building timescales, which is likely of order Myr (similar to the upper bound on Io's surface age (McEwen et al. 2004)), so previous searches were not sensitive enough. Future rotation rate observations will hopefully be able to use a longer baseline and more precise measurements to lower the detection threshold and test the conclusions of this work.

This work draws heavily on Kleer et al. (2019)'s discussion of what Io's interior may be. In particular, their Figure 1.6 sketches four candidate Ios that capture a few key uncertain properties of Io's interior. The range of possible structures feeds into our work because a

magma ocean would significantly change how Io responds to torques, a "magma sponge" would entail a rheologically weak mantle, and where heat is generated in Io will influence its temperature profile and in turn its viscosity profile. The potential for a magma ocean motivates our analysis of what happens if the outer layers of Io are decoupled from the interior. In addition, the possibility of a "magma sponge" means we consider a wide range of interior viscosities, including some quite low for solid rock.

We seek to connect nonsynchronous rotation to Kleer et al. (2019)'s candidate Io models in two ways: First, we can find the range of nonsynchronous rotation periods permitted by their models, constraining the range of rotation rates that are plausible for Io. This allows us to ask whether nonsynchronous rotation can cause volcanoes to be offset. Unfortunately, this turns out to be a fairly weak constraint – there are enough free parameters in the problem that a very wide range of nonsynchronous rotation periods are permitted. In light of this, the primary focus of this work inverts the first question and asks what Io models are possible *if* we treat offset volcanism as a measurement of nonsynchronous rotation with a period of $\sim$1 Myr. If the observed volcanic patterns are caused by nonsynchronous rotation (which is not guaranteed), such rotation should be detectable with future missions. This would provide a strong constraint on the interior, and can potentially allow us to choose between candidate models of Io.

3.1.1 Observational constraints

This work makes use of several existing sets of observations. Most important is Hamilton et al. (2013)'s observation that Io's volcanism, both patera floor units and hotspots, appear to be offset from their expected locations by a few tens of degrees (note that the patera floor units and hotspots do not have identical offsets). Kirchoff et al. (2011) also observe an offset pattern of volcanism, although with a somewhat different distribution. We also use the measurement from Lainey et al. (2009) of Io's $\frac{k_2}{Q}$, derived from observing secular evolution in its orbit and inferring the amount of dissipation taking place. Table 3.1 lists the relevant observational constraints.

A constraint to keep in mind is that Io's surface is very young (McEwen et al. 2004). This is inferred from the lack of impact craters in Galileo imagery. Given that observation, and assumptions about the resurfacing rate, 20 km craters are expected to be erased over a few

Name	Symbol	Value
Dissipation	$\frac{k_2}{Q} = \mathrm{Im}(k_2)$	0.015 ± 0.003
Eccentricity	e	0.0041
Orbital Period	$P = \frac{2\pi}{n}$	1.77 days
Surface Gravity	g	1.789 m/s^2
Density	ρ	3500 kg/m^3
Rigidity	μ	40 GPa

Table 3.1: Io's basic physical and orbital properties. $\frac{k_2}{Q}$ comes from Lainey et al. (2009), and we assume a rigidity that is reasonable for basalt.

hundreds of kyr, and the entire lithosphere is replaced on a timescale of about 10 Myr.

3.2 Methods – No Lithosphere

Io likely consists of a lithosphere overlying a (potentially partially molten) mantle, overlying an iron core (Anderson et al. 2001). In the rest of this work we will generally neglect the core, inclusion of which has no significant effect on our conclusions. A brittle or rigid lithosphere significantly complicates nonsynchronous rotation, so first we analyze the situation where there is no lithosphere and the mantle has uniform properties. This approach has three parts. First, we analytically solve for the relationship between tidal response and rotation rate. Second, we numerically solve for the relationship between interior structure and tidal response. Finally, we explore the parameter space of likely Io interiors and rheological models to find which, if any, are consistent with nonsynchronous rotation on the same timescale as volcano building.

3.2.1 Torque Balance

We begin with the equation for the averaged tidal torque over one orbit from Correia et al. (2014)

$$T = -\frac{3Gm_0^2R^5}{2a^6}\sum_{k=-\infty}^{\infty}\left(X_k^{-3,2}(e)\right)^2 k_2(\omega_k)\sin\left(\delta(\omega_k)\right) \tag{3.1}$$

This is their equation 43 with C (the polar moment of inertia) removed from the denominator to clarify that it is a torque. G is the gravitational constant, m_0 is the mass of

the central body, R is the radius of the orbiting body, and a is the orbital semi-major axis. $X_k^{-3,2}$ are Hansen coefficients, which capture the fact that the torques on an eccentric body vary over its orbit, and they are analytically known functions of eccentricity. Hansen coefficients allow us to treat the torques from an eccentric orbit as an infinite sum of torques from circular orbits (see Hughes (1981) for their recurrence relations and Comstock and Bills (2003) and Correia and Valente (2022) for modern demonstrations of their potential). $k_2(\omega_k)$ are Love Numbers, which describe how strongly the orbiting body is deformed by tides, and are frequency-dependent. $\delta(\omega_k)$ is the tidal 'lag angle', the angle between the orbiting satellite's actual tidal bulge and the direction that tides are trying to point the tidal bulge, which is the satellite-planet axis. The lag angle represents how dissipative the body is. It is strongly frequency dependent, and is equal to $\frac{1}{2Q(|\omega_k|)}$, the tidal 'quality factor' (Macdonald 1964). ω_k describe the frequency spectrum that the tides are being expanded in and they are $\omega_k = 2\Omega - kn$ where Ω is the satellite rotational frequency, k is an integer, and n is the orbital frequency. Because we are concerned with the small difference between synchronous rotation and almost-synchronous rotation, we are particularly interested in the behavior of $\omega_2 = 2(\Omega - n)$, which is zero for synchronous rotation and very small for slightly non-synchronous rotation.

To explore equilibrium behavior, we set $T = 0$, and pull ω_2 out of the sum

$$-\left(X_2^{-3,2}(e)\right)^2 \frac{k_2(\omega_2)}{Q(\omega_2)} = \sum_{k\neq 2} \left(X_k^{-3,2}(e)\right)^2 \frac{k_2(\omega_k)}{Q(\omega_k)} \tag{3.2}$$

The Hansen coefficients are strong functions of eccentricity, so if we expand them and then only keep terms up to second order in eccentricity, most of the terms drop out. and we are only left with $1 \leq k \leq 3$ Here we also note that because Ω and n are extremely close, $\Omega - n \ll \Omega$, so we call $\Omega - n \equiv \omega_{\rm NSR}$, and we simplify $2\Omega - n \approx n$ and $2\Omega - 3n \approx -n$. We use $k_2(n) = k_2(-n)$ and $\delta(n) = -\delta(-n)$. This gives us

$$-(1-5e^2)\frac{k_2(2\omega_{\rm NSR})}{Q(2\omega_{\rm NSR})} = \frac{1}{4}e^2\frac{k_2(n)}{Q(n)} - \frac{49}{4}e^2\frac{k_2(n)}{Q(n)} + O(e^4) \tag{3.3}$$

$$\frac{k_2(2\omega_{\rm NSR})}{Q(2\omega_{\rm NSR})} = 12e^2\frac{k_2(n)}{Q(n)} \tag{3.4}$$

This final equation is powerful. Astrometric measurements of Io's orbital evolution (Lainey et al. 2009) mean that we know at its orbital period, $\frac{k_2(n)}{Q(n)}$ is roughly 0.015, which means that Io will rotate nonsynchronously at whatever frequency makes $\frac{k_2(\omega_{\rm NSR})}{Q(\omega_{\rm NSR})} = 3\times10^{-6}$. More generally, any low-eccentricity body will rotate nonsynchronously with whatever frequency satisfies this equation, and the Hansen coefficient expansion can easily be taken to higher degrees for higher eccentricity bodies.

3.2.2 Rheology

Io will rotate nonsynchronously at whatever frequency makes its $\frac{k_2(\omega)}{Q(\omega)}$ equal to 3×10^{-6}. Finding that frequency requires understanding Io's rheology, a primary goal of this work. At the long periods expected for NSR, k_2 is of order unity, so we are mostly just solving for what frequency makes $Q\approx10^6$. This depends on two things: 1) What is Io's interior composition and temperature structure? 2) What rheological model best describes Io? We need a rheological model because we are extrapolating to periods much longer than any that have been experimentally measured. This extrapolation is a danger in this work; for example dissipation mechanisms may just be fundamentally different at very long periods, but is unavoidable without much longer period empirical constraints.

Question 1 is uncertain, but as discussed in the introduction, Kleer et al. (2019) outline the broad strokes of Io's likely interiors, and distinguishing between the different possibilities they lay out is the main thing needed to predict nonsynchronous rotation. This is also where the converse question enters: if understanding Io's interior can predict its rotation rate, measuring Io's rotation rate can predict its interior.

Question 2 is more challenging because different authors prefer different models (for example, Ross and Schubert (1986), Moore (2003), and Tyler et al. (2015) use a Maxwell rheology for Io, Bierson and Nimmo (2016) use an Andrade rheology for Io, and Jackson et al. (2010) use an Extended Burgers model for laboratory measurements) and the choice of model

has significant impact on our results. We explore the role of rheological models in Section 3.3.1. In this work we primarily focus on Maxwell and Andrade models, discussed in detail in Bierson and Nimmo (2016). Maxwell is the simplest realistic viscoelastic model, it is commonly used in the literature, and it provides a baseline for our results. Andrade, on the other hand, typically provides better fits to observations than Maxwell in both laboratory rheological experiments (e.g Gribb and Cooper 1998) and previous work on Io specifically (Bierson and Nimmo 2016). These better fits come at the cost of higher complexity and more free parameters.

In general, we first compute the body's $k_2(\omega)$ based on a particular layered interior and the associated shear modulus layering. To incorporate the frequency dependence of viscoelastic behavior, we use a complex shear modulus, $\mu^*(\omega)$, in place of a regular shear modulus. This gives us a complex $k_2^*(\omega)$, which has the useful properties (Zschau 1978):

$$\mathrm{Re}\left(k_2^*(\omega)\right) = k_2(\omega) \tag{3.5}$$

$$\mathrm{Im}\left(k_2^*(\omega)\right) = \frac{k_2(\omega)}{Q(\omega)} \tag{3.6}$$

The complex shear modulus is given by first computing a complex compliance (Bierson and Nimmo 2016):

$$\mu^*(\omega) = \frac{1}{J^*(\omega)} = \frac{1}{J_1(\omega) - iJ_2(\omega)} \tag{3.7}$$

where i is the imaginary unit. In the case of a Maxwell rheology

$$J_1(\omega) = \frac{1}{\mu} \tag{3.8}$$

$$J_2(\omega) = \frac{1}{\omega\eta} \tag{3.9}$$

for real shear modulus μ, frequency ω, and viscosity η. Notably, in the high frequency limit, $J_2 \to 0 \implies \mu^* \to \mu$, giving purely elastic behavior, and in the low frequency limit, $J_2 \to \infty \implies \mu^* \to i\omega\eta$, giving purely viscous behavior. For an Andrade rheology, we instead have

Parameter	Value
β	2×10^{-12} $\mathrm{Pa}^{-1}\mathrm{s}^{-\alpha}$
α	0.25
E_b	7×10^5 J/mol
T	1400 K
T_r	1374 K

Table 3.2: Baseline parameters used in Andrade models. These are chosen to match Figure 1 in Bierson and Nimmo (2016), which in turn draws heavily on Jackson et al. (2010).

$$J_1(\omega) = \frac{1}{\mu} + \beta(\omega\lambda)^{-\alpha}\Gamma(\alpha+1)\cos\left(\frac{\alpha\pi}{2}\right) \tag{3.10}$$

$$J_2(\omega) = \frac{1}{\omega\lambda\eta} + \beta(\omega\lambda)^{-\alpha}\Gamma(\alpha+1)\sin\left(\frac{\alpha\pi}{2}\right) \tag{3.11}$$

$$\lambda \equiv \exp\left(\frac{E_b}{R_g}\left(\frac{1}{T_r} - \frac{1}{T}\right)\right) \tag{3.12}$$

where β describes the magnitude of anelasticity and α determines its timescale, Γ is the gamma function, E_b is the activation energy, R_g is the gas constant, T_r is a reference temperature, and T is the actual temperature. With $0 < \alpha < 1$, the high and low frequency limits are the same as in the Maxwell case, but the behavior at frequencies near the Maxwell time ($=\eta/\mu$) can be quite different.

A variety of additional models exist, each preferred by different authors (for example (Jackson et al. 2010) prefer Extended Burgers), where the primary difference is what anelastic behavior should be added to a Maxwell model, as well as whether multiple viscous elements should be included. In this paper we do not explore the diversity of models available, because ultimately we find the elastic lithosphere controls rotation, not viscoelasticity. In the event of a very weak lithosphere, a full treatment of this problem should consider other viscoelastic models.

3.2.3 Interior Models

We are equipped to test arbitrarily layered Io models, but we end up not needing to explore layered structures very deeply. We find that a small number of layers generally reproduces the same results as a larger number of layers. Fewer layers allows much faster

computation, and when we add a magma ocean, having many layers causes numerical noise to blow up, so in this paper we only use enough layers to capture the Io model we care about. Generally that means a rigid surface layer, and a softer interior layer or two. See Figure B.1 for a figure demonstrating this.

Broadly, we want to explore the Io interior candidates outlined in Kleer et al. (2019). Models are assumed to possess a uniform mantle and sometimes a rigid lithosphere. The mantle has a density of 3500 kg/m^3 and a baseline rigidity of 40 GPa.

To explore parameter space, first we test the impact of adjusting the viscosity of the interior, which allows us to assess the impact of different temperature interiors. We extend this to very low viscosities in order to begin to test the impact of a magma ocean directly. This should also cover the behavior of a "magma sponge", although exactly where in the viscosity progression such a scenario should fit is not obvious.

3.2.4 Computing tidal response

With a rheology model and an interior structure chosen, we can proceed to compute a tidal response. In particular, we want to compute the period dependence of $\frac{k_2(\omega)}{Q(\omega)}$, which is a property of the composition and rheological properties of the body of interest. For a uniform or two-layer body, we use the analytical solution in the appendix of Harrison (1963) with complex rigidities. For a general layered body, the problem needs to be solved numerically, which we do using propagator matrices (Sabadini and Vermeersen 2004). This approach uses the fact that in an individual layer, the tidal response can be solved analytically. However, because the layers interact, one layer's response is the next layer's boundary condition (and vice versa), so the entire body needs to be solved simultaneously. We have multiple computer codes to perform this that are benchmarked against each other.

The primary code we use is written in Mathematica, which enables substantial flexibility in mixing analytical and numerical approaches. It is the code used in Bills et al. (2008), modified to handle viscoelasticity through a complex shear modulus using the approach in Equations 3.5-3.12. We benchmark this code against two others: the python code used in Bierson and Nimmo (2016) (in turn based on Roberts and Nimmo (2008)), and the fortran code used in Moore and Schubert (2000). The Bierson and Nimmo (2016) code has the advantage of being designed for an Andrade rheology, so it can explicitly test those cases. The Moore and

Schubert (2000) code is designed to handle the modified boundary conditions necessary to include a fluid layer, so is useful for checking our magma ocean cases. Our primary code cannot properly handle a fluid layer, and instead we approximate it by lowering the rigidity and viscosities, so we check it against the code from Moore and Schubert (2000) to ensure that approximation is accurate.

In addition, we benchmark our Mathematica code against Harrison (1963)'s analytical two-layer results (based on work by Kaula (1963)). The two-layer numerical results agree well with what we expect analytically.

3.3 Results – No Lithosphere

3.3.1 Rheology Model and Temperature Dependence

Armed with the ability to compute $\frac{k_2(\omega)}{Q(\omega)}$, there are two particular periods we care about. First, we are interested in Io's orbital period, where $\frac{k_2(\omega)}{Q(\omega)}$ has actually been measured (Lainey et al. 2009) as $\frac{k_2(n)}{Q(n)} = 0.015 \pm 0.003$, providing an observational anchor for our models. The second period we care about is whatever period makes $\frac{k_2(\omega)}{Q(\omega)} = 3 \times 10^{-6}$, because that is where we will have nonsynchronous rotation (see Section 3.2.1 above). In Figure 3.1 we plot $\frac{k_2(\omega)}{Q(\omega)}$ for a variety of different models, and these two periods are indicated by the star and by where each curve crosses the horizontal dashed line. Away from dissipation peak(s) (i.e. away from the Maxwell time), we generally see a power law, with a negative slope of one at long periods and a model-dependent positive slope at short periods (either the Andrade α, or one for a Maxwell model). On this plot we can simply read off the nonsynchronous rotation period, the x-coordinate where the curve crosses the dashed line.

Figure 3.1 shows the effects of adjusting a few key parameters in our model. The green curve shows a uniform Maxwellian Io made of Earth upper mantle-like material, with a viscosity of 10^{21} Pa·s and a rigidity of 40 GPa. The light green curve shows a 'canonical' Maxwellian Io, which dials down the viscosity (equivalent to dialing up the temperature) of the mantle to 10^{15} Pa·s in order to fit the k_2/Q constraint (the blue star). Notably, the canonical Maxwell model is very close to the "ruled out" region, meaning that if the lithosphere does turn out to be weak, future spacecraft (and possibly ground based) measurements of Io's

rotation rate can likely test that particular model. Comparing the dark green and orange curves shows the effect of switching between a Maxwell and an Andrade model. Comparing the orange and purple curves shows the effect of a hotter/lower viscosity interior of 10^{18} Pa·s (note that the purple curve is mostly hidden by/matching the pink curve). Switching between the purple and pink curves shows the effect of adding a 10 km rigid lid on top of the mantle, discussed further in Section 3.4. This lithosphere has an effectively infinite viscosity and no ability to relax viscously, unlike the viscous approximation discussed in Section 3.4.1 below.

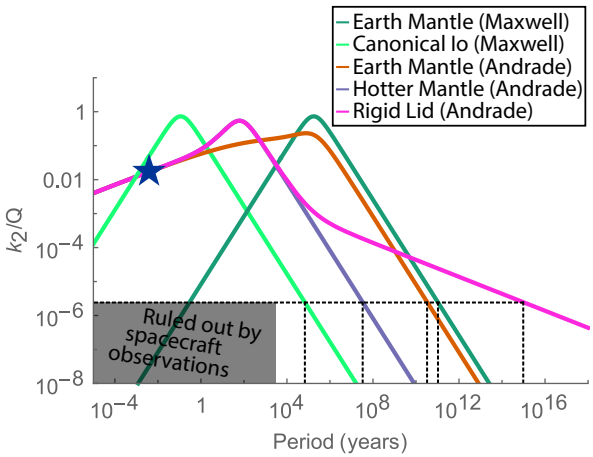

Figure 3.1: The effects of adjusting a few key parameters in our model. The blue star indicates the known orbital value of $\frac{k_2(\omega)}{Q(\omega)}$ from orbital evolution, the horizontal dashed line indicates the necessary $\frac{k_2(\omega)}{Q(\omega)}$ for nonsynchronous rotation, and the vertical dashed lines mark the nonsynchronous rotation period for each model. The gray box indicates the NSR periods that have already been ruled out (Hoppa et al. 1999) by spacecraft observations.

Our choice of rheology model appears to have a strong effect at short periods, where the model determines the power law slope, but little effect at long periods, where all models have a negative unit slope. Because Maxwell models have (±)unit slopes on both sides of their Maxwell times, our single tie-point at the tidal period (the blue star in Figure 3.1) is enough to pin the position of the whole curve and basically fully constrain nonsynchronous rotation if Io is actually a Maxwell material. However, because Andrade rheologies have shallower slopes at short periods, a much wider range of possible viscosities are consistent with the orbital observations, and the long period side of the curve is able to shift more freely in period (i.e. they can be shifted left-right in Figure 3.1). This means that even though long-period behavior

is identical between Maxwell and Andrade rheologies, the rheology model chosen is still important because nonsynchronous rotation depends on the link between long-period and tidal-period dissipation (equation 3.4).

3.3.2 Magma Ocean

A magma ocean significantly impacts a body's tidal response. This is for two reasons – first, it means there is a low-viscosity near-surface layer, which matters for interior Maxwell frequencies, and has the potential to enable additional dissipation mechanisms (e.g. Chen et al. 2014). For our purposes, this is not central, because at very long periods a liquid and a warm enough solid are both well above their Maxwell periods and behave in a fairly similar fashion. In addition to its direct impact on dissipation, a magma ocean can also be important because it may mean that surface layers are mechanically decoupled from interior layers. We discuss this issue further below (Section 3.4.2.1).

In Figure 3.2 we show the first of these two effects by assuming the body is still rotationally coupled, and dialing down the viscosity of the interior of the body to sweep from fully solid to fully liquid. In the upper panel, we show the effect of lowering the viscosity of the interior, below a 10 km thick Earth-mantle-like surface layer. In the lower panel, the 10 km surface layer has the same rigidity but infinite viscosity, simulating a lithosphere. Both layers in both panels are Andrade materials. The fully solid interior is the green curve in Figure 3.2 and corresponds to the orange curve in Figure 3.1. As the interior viscosity is dialed down, the peak corresponding to its response shifts, but the aggregate behavior shows only a small change: The green and orange curves show the fully-solid and fully-liquid limiting behavior, and the fact that they are only moderately separated tells us that at least as long as the shell is rotationally coupled to the interior (which we discuss in Section 3.4.2.1), the presence of a magma ocean is not important for our results. The role of the lithosphere, on the other hand, is crucial and is discussed in more detail below. The fact that almost all the curves intersect the blue star, our one anchor point thanks to astrometry, reflects the fact the astrometric constraint unfortunately does not tell us much beyond supporting an Andrade rheology.

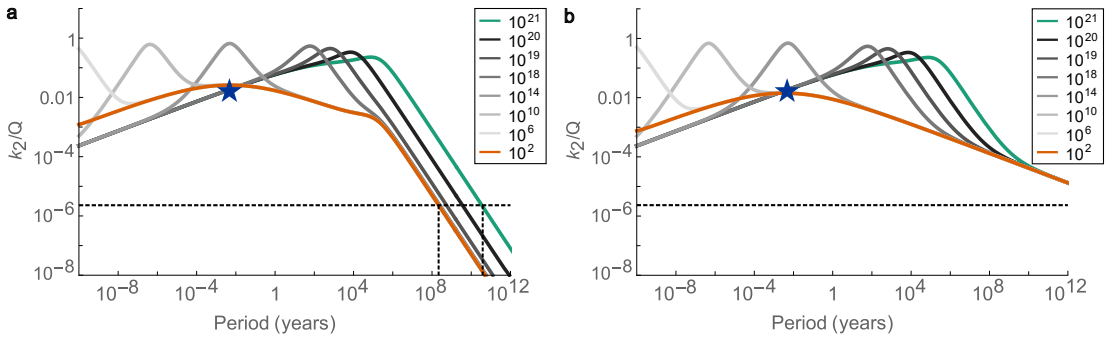

Figure 3.2: Testing a magma ocean by dialing down viscosity, in units of Pa·s. This is a two layer Andrade model, where the interior has the viscosity listed in the legend, and there is a 10 km surface layer that in panel **a** has a viscosity of 10^{21} Pa·s, and in panel **b** has a viscosity of $10^{2100} \approx \infty$ Pa·s. Note the uneven viscosity step size, and the different x-axis range from Figure 3.1. The latter case feeds into our discussion in Section 3.4, where we begin with this case of a rigid lithosphere and explore its strength when the lithosphere is faulted. When we scan by lowering the rigidity instead of the viscosity, or both rigidity and viscosity simultaneously, we get somewhat different intermediate behaviors but the same endmembers. In the panel **b** we do not reach $\frac{k_2(\omega)}{Q(\omega)} = 3 \times 10^{-6}$ until about 10^{15} yr (off the plot), which matches the result in Figure 3.3.

3.4 Effect of a Lithosphere

3.4.1 Method

A strong rigid lid is able to limit Io's deformation (i.e. reduce $\frac{k_2(\omega)}{Q(\omega)}$) and, as discussed later, possibly shut down nonsynchronous rotation entirely. If the lithosphere is unfractured and purely elastic (no brittle or viscous deformation), its response to tidal stresses will dissipate no energy, and will significantly limit the size of the tidal deformation in the interior. However, if the lithosphere is weak, its impact on the tidal response will be diminished – for example, in the case of the Earth, the lithosphere does not play an important role in true polar wander (Tsai and Stevenson 2007), in part because the lithosphere is broken into plates. Below we develop an approach to incorporating the effect of a fractured lithosphere on non-synchronou rotation.

Because we analyze the rotational evolution via $\frac{k_2(\omega)}{Q(\omega)}$, and compute that parameter with viscoelastic tools, incorporating brittle and frictional deformation is challenging. To bridge this, we want to parameterize the role of friction in the lithosphere as though it is a viscosity, by introducing an "effective viscosity". If we assume that the lithosphere can deform by

movement on faults, and faults are widespread, then frictional dissipation on those faults acts like a viscosity if we know the bulk strain rate and the stress on the faults. First, we discuss the effect of a deformable lithosphere in the case of a solid mantle. We then go on to examine the more complicated case of a lithosphere above a magma ocean.

Say the lithosphere has thickness D and is filled with faults of length l with a characteristic spacing between them of d. Then, for Io radius R, there are roughly $\frac{4\pi R^2}{dl}$ total faults, so $\frac{4\pi R^2}{d}$ total fault length and $\frac{4\pi R^2}{d}D$ total fault surface area. If the lithosphere is undergoing a strain rate of $\dot{\epsilon}$ then the velocity on each fault is $d\dot{\epsilon}$. If the resisting stress due to friction is σ (combining the normal stress and the coefficient of friction), the work being done on faults per unit time per area is $\sigma d\dot{\epsilon}$. Then, the power dissipated in the entire lithosphere is $f_1\sigma d\dot{\epsilon} \times \frac{4\pi R^2}{d}D$, where f_1 is a geometric factor to account for our approximate lengths and surface areas. We can describe our effective viscosity η_e as the viscosity which, if the entire lithosphere were undergoing viscous creep, would dissipate the same power. In general, the power dissipated through viscous creep is $\eta\dot{\epsilon}^2 V$ for volume $V = 4\pi R^2 D$, so we can set the frictional and viscous dissipations equal to find

$$\sigma d\dot{\epsilon} D\frac{4\pi R^2}{d} = f_2\eta_e\dot{\epsilon}^2 4\pi R^2 D \tag{3.13}$$

$$\eta_e = f_2\frac{\sigma}{\dot{\epsilon}} \tag{3.14}$$

This reduces to a normal-looking viscosity equation. However, σ here is due to friction – it is the characteristic frictional stress on faults – and $\dot{\epsilon}$ is the relevant strain rate, which is approximately the fractional size of Io's tidal bulge divided by the nonsynchronous rotation period. For polar radius c and tidal axis radius a, Io's bulge size is $\frac{a-c}{a} \approx 10^{-2}$. Note that we only made order-of-magnitude estimates here and this is a very approximate equation. To account for that, we introduced f_2, which accounts for the fact that we are treating frictional dissipation as though it is a viscosity, which is at best approximate, but may introduce a larger error depending on the actual physics it hides.

We then assume $\sigma \approx f_{fric}\rho g\frac{D}{2}$ (using halfway through the lithosphere as a characteristic stress), with a friction coefficient f_{fric}, and allow f_1 from before to include fault angles (both the friction coefficient and fault angles are probably close to order unity), and note that

$\dot{\epsilon} \approx 10^{-2}\omega_{\rm NSR} = \frac{2\pi \times 10^{-2}}{P_{NSR}}$ for NSR period P_{NSR}, then we get

$$\eta_e \approx 10^{17} \times f \times \left(\frac{D}{10 \text{ km}}\right) \times \left(\frac{P_{NSR}}{1 \text{ yr}}\right) \text{ Pa} \cdot \text{s} \tag{3.15}$$

All the numerical factors, f_1, f_2, and f_{fric} are wrapped into a single "lithosphere viscosity factor" f here. The effective viscosity ends up only depending on a few things: the lithosphere thickness; the nonsynchronous rotation rate; (implicitly) the size of Io's tidal bulge; and crucially, our uncertain numerical factor f.

3.4.2 Results

A perfectly elastic, unfractured lithosphere will not dissipate energy at all, and will experience reduced tidal deformation relative to the no-lithosphere case. This limits the amount of deformation in layers below it, and therefore the total amount of dissipation possible in the interior. The pink curve in Figure 3.1 shows this effect. As expected, it shuts down realistic nonsynchronous rotation, causing the nonsynchronous rotation period to be many orders of magnitude longer than the age of the solar system.

However, a realistic lithosphere will be fractured, and motion on faults will allow both more deformation and more dissipation. As discussed in Section 3.4.1, we can parameterize fault motion as a viscosity, and use this value as an input parameter for our tidal response models. Before exploring the numerical results, note that we should expect non-intuitive behavior. This is because 1) the nonsynchronous rotation rate depends on the lithosphere's viscosity (for example, compare the two Maxwell curves in Figure 3.1 to see the effect of mantle viscosity), and 2) the effective viscosity depends on the nonsynchronous rotation rate (as is shown in Equation 3.15). In short: NSR period is roughly proportional to viscosity, and our effective viscosity is linearly proportional to NSR period. The equilibrium NSR period is strongly dependent on the uncertain factor f in Equation 3.15, so the interplay between NSR period and viscosity is expected to be very strongly dependent on f. If it is small, the effective viscosity of the lithosphere will be small at NSR periods, and the lithosphere will easily move. If, on the other hand, f is large, the lithosphere will appear strong at NSR periods, and the lithosphere will control those NSR periods. f effectively acts like a switch; when it is small,

the lithosphere is invisible, and when it is large, the lithosphere behaves as though it is unfractured. This effect is illustrated in Figure 3.3. Here we self-consistently solve for the nonsynchronous rotation rate by simultaneously solving both the rotation rate (equation 3.4) and viscosity equation (equation 3.15), and plot it as a function of f and lid thickness. Figure 3.3 shows the crucial importance of this unknown parameter f: If it is smaller than about 10^{-5}, the lithosphere is irrelevant to nonsynchronous rotation and the deeper interior determines the NSR rate; if it is larger, there is no nonsynchronous rotation. We discuss the likely value of f further below.

In Figure 3.3 we also include the same calculation for Earth parameters, to illustrate the crucial importance of gravity and radius in whether the lithosphere is able to suppress dissipation. True polar wander on Earth has a similar timescale and total strain to our hypothetical NSR on Io, so one might expect either both or neither to be possible. However, due to Earth's larger size (and thus larger surface gravity), there is no contradiction between the apparent ease of true polar wander on Earth, and the difficulty of non-synchronous rotation on Io.

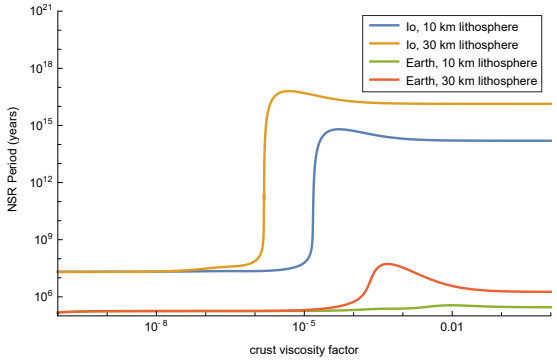

Figure 3.3: Solving for the nonsynchronous rotation period when a "lithosphere" is included by giving the top layer the viscosity in Equation 3.15 – equivalent to finding the intersection between the response curves and the dashed line in Figure 3.1 when the viscosity is allowed to vary with period. The x-axis is f from Equation 3.15. The viscosity and the rotation rate depend on each other, so we solve for them simultaneously to find a self-consistent result. All these models use an Andrade rheology. The blue and yellow curves are Io for two different lithosphere thicknesses, and what we can see is that for f anywhere near unity, the lithosphere shuts down meaningful nonsynchronous rotation (i.e. 10^{10} yr on the y-axis is less than one extra rotation over the age of the solar system). Notably, this would not be the case if Io was much larger – the red and green curves are made by substituting in Earth's radius and surface gravity (but the body is still in Io's orbital configuration), and we see that Earth's larger size makes rigidity much less important.

3.4.2.1 Decoupled Shell

A major complication to this work comes from the fact that so far, we have assumed that the body rotates uniformly. If, instead, the surface is decoupled from the interior and can rotate at a different rate, we need to consider the rotation of that shell alone. Goldreich and Mitchell (2010) explore the torque balance on a decoupled shell, so we work from their approach.

Broadly, two important processes make up the decoupled shell situation. First, instead of a whole body, the relevant gravitational torques are only coupled to the smaller shell so they are weaker, but this is offset by the moment of inertia of the shell also being smaller than the whole body. For Io, the result is a modestly different torque balance, but overall a similar situation. Second, when the shell rotates over the interior, it needs to deform: the tidal shape of the interior is effectively fixed, and the shell needs to change shape to accommodate this as it rotates. If the shell has substantial rigidity, there will be a large elastic resistance to this deformation, making rotation hard; if the shell behaves mostly like a fluid (because gravity is strong), it will be relatively easy for it to change shape as it rotates over the interior. Goldreich and Mitchell (2010) identify a parameter that they (and we) call $\mathcal{R}$ which captures this, and for Io it is ≈ 0.1, so elasticity is (marginally) unimportant in the shell's ability to decouple.

To analyze this quantitatively, first we follow Goldreich and Mitchell (2010)'s assumption that their $\mathcal{R}$ parameter (introduced in their equation 11) is small, because although it is closer to unity for Io than Europa, the long periods we are concerned with mean the lithosphere is effectively thinner and will reduce $\mathcal{R}$. Although they look different, equations 14 and 15 of Goldreich and Mitchell (2010) are very similar to Correia et al. (2014)'s calculation at $k = 1$ and $k = 3$. We show in the Appendix that

$$\ddot{\theta}_{G\&M} = \frac{h_2(n)}{h_f} \frac{50}{\ln\left(\frac{n}{\omega_{\rm NSR}}\right)} \ddot{\theta}_{Correia} \tag{3.16}$$

where h_2 is the shape Love number and h_f is it in the fluid limit (i.e. at very long periods). Here $\ddot{\theta}$ is the angular acceleration, the torque divided by the moment of inertia, and the

difference arises because Goldreich and Mitchell (2010) consider a decoupled shell while Correia et al. (2014) do not. This simple relationship results from a lot of cancellation, including the fact that, for a thin shell, both the torque on a shell and the shell's moment of inertia depend linearly on its thickness. The $\frac{h_2(\omega)}{h_f}$ term appears because the shell needs to deform as it rotates over the interior, and h_2 represents its ability to deform. The $\ln\left(\frac{n}{\omega_{\rm NSR}}\right)$ term captures the fact that lithosphere is effectively thinner on long timescales – the longer you wait, the lower the temperature a material needs to be to deform viscously – and this term captures the thickness difference between the long and short period lithospheres. $\frac{h_2(\omega)}{h_f}\frac{50}{\ln\left(\frac{n}{\omega_{\rm NSR}}\right)}$ is model dependent, but broadly $\frac{h_2(n)}{h_f}$ is of order 10^{-1} and $\frac{50}{\ln\left(\frac{n}{\omega_{\rm NSR}}\right)} \approx 2$. Therefore it will lower the necessary $\frac{k_2(\omega_{\rm NSR})}{Q(\omega_{\rm NSR})}$ by about one order of magnitude, so from 3×10^{-6} to 3×10^{-7}. Other things being equal, this will increase the nonsynchronous rotation period by the same factor. The main difference introduced by a decoupled shell, and the reason h_2 (describing shape, rather than gravitational potential) enters, is the fact that the shell needs to deform relative to the interior – its physical shape matters rather than just its gravitational potential, because the shell and interior ellipsoids must have their shapes conform as they rotate differentially.

3.5 Discussion

3.5.1 Rigid Lid

Given that what we are calling the "lithosphere viscosity factor" f (plotted in Figure 3.3) has fairly little physical grounding, it is hard to justify it being far from unity, although it certainly could be. This strongly suggests that the presence of any lithosphere, even a highly faulted one, will prevent nonsynchronous rotation on Io.

Note that, in principle, this analysis is not unique to Io, and broadly should apply similarly to true polar wander on Earth. Earth's true polar wander period is roughly 100 Myr (Tsai and Stevenson 2007), has amplitudes of many tens of degrees, and is overcoming a rotational/tidal flattening of a similar amplitude to that of Io. However, as we show in Figure 3.3, Earth and Io's lithospheres have very different abilities to suppress dissipation. This is primarily controlled by surface gravity, which is such a strong effect that even with less than one order of magnitude difference in gravity, Earth and Io have predicted relaxation rates that differ by

several orders of magnitude.

The strength of the lithosphere is the most important variable in this work. If Io's lithosphere behaves as a globally coherent rigid layer, nonsynchronous rotation will not occur. If the lithosphere is sufficiently weak, as is the case on Earth (Tsai and Stevenson 2007), the nonsynchronous rotation rate will depend on the viscosity of Io's interior and may be observable. We do not see a reason for it to be weak (equivalently, for f to be much less than unity), and models of fault-derived topography on Io suggest a lithosphere capable of supporting stresses of hundreds of MPa (Bland and Mckinnon 2016), but it is too early to rule out a weak lithosphere entirely. More detailed explorations of how faults behave under Io conditions is necessary to determine the lithosphere's actual strength.

One mechanism to relieve stress that we have not explored in detail is the fact that Io's lithosphere is advecting downward (Kirchoff et al. 2011), and once material gets deep enough it will release any accumulated elastic stress. Shallower lithosphere material will need to take up this stress, increasing the elastic strain, until that material also heats up and releases it. This mechanism is only likely to relieve the small tidal lag angle on ∼Myr timescales (the lithospheric turnover timescale), so it may serve to place an upper bound on the timescale found in Section 3.4.1.

It is also possible that Io's surface and its interior are able to rotate independently, and our observations of the surface will only sample the behavior of the outer shell. This decoupling has a roughly 1 order of magnitude effect on the expected rate of nonsynchronous rotation, causing it to be moderately slower. This will be important for interpreting observations if nonsynchronous rotation does occur, but relatively minor compared to the question of whether the lithosphere allows nonsynchronous rotation at all.

3.5.2 Nonsynchronous rotation rates

If the lithosphere is in fact weak, nonsynchronous rotation is likely and will depend on the temperature structure of Io's mantle.

If Io's interior is Maxwellian, it must have a viscosity near 10^{15} Pa·s, which is how it is often modeled (discussed by Bierson and Nimmo (2016)). This viscosity would lead to a nonsynchronous rotation periods of order 10^5 years. This is too fast to explain the observed offset of volcanic features, but would likely be detectable with the next mission to Io.

If, as seems likely, the interior is non-Maxwellian, for example if it has Andrade behavior, it is able to be colder/higher viscosity while still satisfying the measured k_2/Q. If it is moderately higher viscosity, with a value in the vicinity of 10^{18} Pa·s, nonsynchronous rotation will occur on a timescale similar to that of volcano building. Nonsynchronous rotation in this case will be harder to detect, and may require a mission to be designed carefully to detect slow nonsynchronous rotation. If Io's volcano offset is a result of nonsynchronous rotation, its interior viscosity is likely close to 10^{18} Pa·s which in turn constrains its thermal state. This viscosity value is not unreasonable, given that the warmest (and water-rich) regions of the Earth's upper mantle have viscosities in the range 10^{18-19} Pa s (e.g. Dixon et al. 2004). If Io's interior is even colder, with a viscosity closer to Earth's upper mantle, nonsynchronous

rotation will be slow, irrelevant to volcano building, and will probably be undetectable. Note, however, that all these scenarios presume a weak lithosphere.

The presence of a magma ocean has fairly little direct impact on nonsynchronous rotation. However, if it allows Io's shell to rotationally decouple from the interior, it will probably slow the nonsynchronous rotation rate by a factor of about 10, as discussed in Section 3.4.2.1.

3.5.3 Europa

This work focused on Io, but Europa is also a compelling place to look for nonsynchronous rotation. It has a less rigid crust and a shell that is known to be decoupled from the interior, opening up a similar but slightly different region of parameter space. It is beyond the scope of this work, but applying similar techniques to Europa is likely valuable. It is probable that the behavior of faults will again be important, so an understanding of the behavior of icy faults will be essential for a full treatment of Europa.

3.6 Conclusions

On Io, the presence of an elastic/brittle lithosphere is the primary control of nonsynchronous rotation. A detailed analysis of how faults can support tidal stresses on Io is beyond the scope of this work, so we approximate this behavior by parameterizing fault movement as a viscosity. We find that Io's lithosphere is probably very strong, and should be able to fully suppress nonsynchronous rotation. A productive next step to confirm this behavior would be more focused modelling of the behavior of a lithosphere under these conditions – a finite element lithosphere model, or another similar model that can realistically assess how a fractured lithosphere will behave, is likely the best way to assess its strength on these timescales.

Barring lithospheric fault behavior that we miss with our simple model, we expect Io's lithosphere to be relatively strong. This will prevent nonsynchronous rotation, regardless of the rheology of the interior (including whether it is molten) or the ability of the lithosphere to rotate independently.

If it does turn out that the lithosphere is weak, nonsynchronous rotation should occur, and its rate will be directly determined by Io's typical mantle temperature. If Io's volcano

distribution is influenced by nonsynchronous rotation, its mantle viscosity is of order 10^{18} Pa s, comparable to the lowest mantle viscosities seen for Earth. If Io has a decoupled surface layer, this viscosity is that of the upper layer's ductile region.

Bibliography

Abrahams, Jacob N. H. and Francis Nimmo (2019). "Ferrovolcanism: Iron Volcanism on Metallic Asteroids". In: *Geophysical Research Letters* 46, 2019GL082542. DOI: 10.1029/2019GL082542.

Abrahams, Jacob N H, Francis Nimmo, Ian Garrick-bethell, and Bruce G Bills (2022). "A theoretical investigation of non-synchronous rotation on Io". In: *In Review*.

Abrahams, Jacob N.H., Francis Nimmo, Tracy M. Becker, G. Randall Gladstone, Kurt D. Retherford, Gregor Steinbrügge, and Erwan Mazarico (2021). "Improved Determination of Europa's Long-Wavelength Topography Using Stellar Occultations". In: *Earth and Space Science* 8.7. DOI: 10.1029/2020EA001586.

Ahrens, Thomas J and Mary L Johnson (1995). "Shock Wave Data for Minerals". In: *Minereral Physics & Crystallography: A handbook of Physical Constants* 2, pp. 143–184.

Anderson, John D., Robert A. Jacobson, Eunice L. Lau, William B. Moore, and Gerald Schubert (2001). "Io's gravity field and interior structure". In: *Journal of Geophysical Research: Planets* 106.E12, pp. 32963–32969. DOI: 10.1029/2000JE001367.

Araki, H. et al. (2009). "Lunar global shape and polar topography derived from Kaguya-LALT laser altimetry". In: *Science* 323.5916, pp. 897–900. DOI: 10.1126/science.1164146.

Ashby, M. F. (1999). *Materials selection in mechanical design*. Oxford, England: Butterworth-Heinemann.

Asphaug, Erik, Craig B. Agnor, and Quentin Williams (2006). "Hit-and-run planetary collisions". In: *Nature* 439.7073, pp. 155–160. DOI: 10.1038/nature04311.

Beuthe, Mikael (2013). "Spatial patterns of tidal heating". In: *Icarus* 223.1, pp. 308–329. DOI: 10.1016/j.icarus.2012.11.020.

Bierson, C. J. and F. Nimmo (2016). "A test for Io's magma ocean: Modeling tidal dissipation with a partially molten mantle". In: *Journal of Geophysical Research: Planets* 121.11, pp. 2211–2224. DOI: 10.1002/2016JE005005.

Bills, B G, R R Ghent, D W Leverington, and F Nimmo (2008). "Internal Structure of Mars: Viscosity Constraints from Short Period Tides and Loads". In: *39th Lunar and Planetary Science Conference* 39.2008, p. 2016.

Bland, Michael T. and William B. Mckinnon (2016). "Mountain building on Io driven by deep faulting". In: *Nature Geoscience* 9.6, pp. 429–432. DOI: 10.1038/ngeo2711.

Blankenship, Donald et al. (2018). "REASON for Europa". In: *42nd COSPAR Scientific Assembly*. Vol. 42, B5.3–55–18.

Bottke, William F., Daniel D. Durda, David Nesvorný, Robert Jedicke, Alessandro Morbidelli, David Vokrouhlický, and Hal Levison (2005). "The fossilized size distribution of the main asteroid belt". In: *Icarus* 175.1, pp. 111–140. DOI: 10.1016/j.icarus.2004.10.026.

Bower, Sally M and Andrew W Woods (1997). "Control of magma volatile content on the mass erupted during explosive volcanic eruptions". In: *Journal of Geophysical Research* 102, pp. 10273–10290. DOI: 10.1029/96JB03176.

Bryson, James F J, Claire I O Nichols, Julia Herrero-Albillos, Florian Kronast, Takeshi Kasama, Hossein Alimadadi, Gerrit Van Der Laan, Francis Nimmo, and Richard J Harrison (2015). "Long-lived magnetism from solidification-driven convection on the pallasite parent body". In: *Nature* 517.7535, pp. 472–475. DOI: 10.1038/nature14114.

Carslaw, H. S. and J. C. Jaeger (1959). *Conduction of Heat in Solids*. 2nd. Oxford, England: Clarendon Press.

Chabot, Nancy L. and Henning Haack (2006). "Evolution of Asteroidal Cores". In: *Meteorites and the Early Solar System II* April, pp. 747–771.

Chen, E. M. A., Francis Nimmo, and Gary A Glatzmaier (2014). "Tidal heating in icy satellite oceans". In: *Icarus* 229, pp. 11–30. DOI: 10.1029/2009GL038300.

Comstock, Robert L. and Bruce G. Bills (2003). "A solar system survey of forced librations in longitude". In: *Journal of Geophysical Research E: Planets* 108.9. DOI: 10.1029/2003je002100.

Correia, Alexandre C.M., Gwenaël Boué, Jacques Laskar, and Adrián Rodríguez (2014). "Deformation and tidal evolution of close-in planets and satellites using a Maxwell

viscoelastic rheology". In: *Astronomy and Astrophysics* 571, pp. 1–16. DOI: 10.1051/0004-6361/201424211. arXiv: 1411.1860.

Correia, Alexandre C.M. and Ema F.S. Valente (2022). "Tidal evolution for any rheological model using a vectorial approach expressed in Hansen coefficients". In: *Celestial Mechanics and Dynamical Astronomy* 134.3, pp. 1–37. DOI: 10.1007/s10569-022-10079-3.

Crawford, Glen D. and David J. Stevenson (1988). "Gas-driven water volcanism and the resurfacing of Europa". In: *Icarus* 73.1, pp. 66–79. DOI: 10.1016/0019-1035(88)90085-1.

Dixon, Jacqueline E., T. H. Dixon, D. R. Bell, and R. Malservisi (2004). "Lateral variation in upper mantle viscosity: Role of water". In: *Earth and Planetary Science Letters* 222.2, pp. 451–467. DOI: 10.1016/j.epsl.2004.03.022.

Ermakov, A. I., R. R. Fu, J. C. Castillo-Rogez, C. A. Raymond, R. S. Park, F. Preusker, C. T. Russell, D. E. Smith, and M. T. Zuber (2017). "Constraints on Ceres' Internal Structure and Evolution From Its Shape and Gravity Measured by the Dawn Spacecraft". In: *Journal of Geophysical Research: Planets* 122.11, pp. 2267–2293. DOI: 10.1002/2017JE005302.

Ermakov, Anton I., Mikhail A. Kreslavsky, Jennifer E.C. Scully, Kynan H.G. Hughson, and Ryan S. Park (2019). "Surface Roughness and Gravitational Slope Distributions of Vesta and Ceres". In: *Journal of Geophysical Research: Planets* 124.1, pp. 14–30. DOI: 10.1029/2018JE005813.

Frost, H. J. and M. F. Ashby (1982). *Deformation-mechanism maps: The plasticity and creep of metals and ceramics*. Oxford, England: Pergamon Press.

Fu, Roger R. et al. (2017). "The interior structure of Ceres as revealed by surface topography". In: *Earth and Planetary Science Letters* 476, pp. 153–164. DOI: 10.1016/j.epsl.2017.07.053.

Fulton, P. M., E. E. Brodsky, Y. Kano, J. Mori, F. Chester, T. Ishikawa, R. N. Harris, W. Lin, N. Eguchi, and S. Toczko (2013). "Low coseismic friction on the Tohoku-Oki fault determined from temperature measurements". In: *Science* 342.6163, pp. 1214–1217. DOI: 10.1126/science.1243641.

Goldreich, Peter M. and J. L. Mitchell (2010). "Elastic ice shells of synchronous moons: Implications for cracks on Europa and non-synchronous rotation of Titan". In: *Icarus* 209.2, pp. 631–638. DOI: 10.1016/j.icarus.2010.04.013.

Goldstein, J. I., E. R.D. Scott, and N. L. Chabot (2009). "Iron meteorites: Crystallization, thermal history, parent bodies, and origin". In: *Chemie der Erde* 69.4, pp. 293–325. DOI: 10.1016/j.chemer.2009.01.002.

Greenberg, Richard and Stuart J. Weidenschilling (1984). "How fast do Galilean satellites spin?" In: *Icarus* 58.2, pp. 186–196. DOI: 10.1016/0019-1035(84)90038-1.

Gribb, Tye T and Reid F Cooper (1998). "Low-frequency shear attenuation in polycrystalline olivine: Grain boundary diffusion and the physical significance of the Andrade model for viscoelastic rheology". In: *Journal of Geophysical Research* 103, pp. 27267–27279. DOI: 10.1029/98JB02786.

Grima, Cyril, Donald D. Blankenship, and Dustin M. Schroeder (2015). "Radar signal propagation through the ionosphere of Europa". In: *Planetary and Space Science* 117, pp. 421–428. DOI: 10.1016/j.pss.2015.08.017.

Haack, Henning, Kaare L Rasmussen, and Paul H Warren (1990). "Effects of Regolith / Megaregolith Insulation on the Cooling Histories of Differentiated Asteroids". In: *Journal of Geophysical Research: Solid Earth Banner* 95, pp. 5111–5124. DOI: 10.1029/JB095iB04p05111.

Haack, Henning and Edward R. D. Scott (2009). "Asteroid core crystallization by inward dendritic growth". In: *Journal of Geophysical Research* 97.E9, pp. 14727–14734. DOI: 10.1029/92je01497.

Hamilton, Christopher W., Ciarán D. Beggan, Susanne Still, Mikael Beuthe, Rosaly M.C. Lopes, David A. Williams, Jani Radebaugh, and William Wright (2013). "Spatial distribution of volcanoes on Io: Implications for tidal heating and magma ascent". In: *Earth and Planetary Science Letters* 361, pp. 272–286.

Harrison, J. C. (1963). "An analysis of the lunar tides". In: *Journal of Geophysical Research* 68.14, pp. 4269–4280. DOI: 10.1029/jz068i014p04269.

Head, James W. and Lionel Wilson (1992). "Lunar mare volcanism: Stratigraphy, eruption conditions, and the evolution of secondary crusts". In: *Geochimica et Cosmochimica Acta* 56.6, pp. 2155–2175. DOI: 10.1016/0016-7037(92)90183-J.

Hemingway, D., F. Nimmo, H. Zebker, and L. Iess (2013). "A rigid and weathered ice shell on Titan". In: *Nature* 500.7464, pp. 550–552. DOI: 10.1038/nature12400.

Hemingway, Douglas J. and Tushar Mittal (2019). "Enceladus's ice shell structure as a window on internal heat production". In: *Icarus* 332, pp. 111–131. DOI: 10.1016/j.icarus.2019.03.011.

Hevey, P J and I S Sanders (2006). "A model for planetisemal meltdown by 26Al and its implications for meteorite parent bodies". In: *Meteoritics & Planetary Science* 41.1, pp. 95–106. DOI: https://doi.org/10.1111/j.1945-5100.2006.tb00195.x.

Hoppa, Gregory, Richard Greenberg, Paul Geissler, B. Randall Tufts, J. Plassmann, and Daniel D. Durda (1999). "Rotation of Europa: Constraints from Terminator and Limb Positions". In: *Icarus* 137.2, pp. 341–347. DOI: 10.1006/icar.1998.6065.

Hughes, S. (1981). "The computation of tables of Hansen coefficients". In: *Celestial Mechanics* 25.1, pp. 101–107. DOI: 10.1007/BF01301812.

Hutchison, R. (2004). *Meteorites: A petrologic, chemical and isotopic synthesis*. Cambridge, England: Cambridge University Press.

Iess, L. et al. (2014). "The gravity field and interior structure of Enceladus". In: *Science* 344.6179, pp. 78–80. DOI: 10.1126/science.1250551.

Jackson, Ian, Ulrich H. Faul, Daisuke Suetsugu, Craig Bina, Toru Inoue, and Mark Jellinek (2010). "Grainsize-sensitive viscoelastic relaxation in olivine: Towards a robust laboratory-based model for seismological application". In: *Physics of the Earth and Planetary Interiors* 183.1-2, pp. 151–163. DOI: 10.1016/j.pepi.2010.09.005.

Jellinek, A. Mark and Donald J. DePaolo (2003). "A model for the origin of large silicic magma chambers: Precursors of caldera-forming eruptions". In: *Bulletin of Volcanology* 65.5, pp. 363–381. DOI: 10.1007/s00445-003-0277-y.

Karato, Shun Ichiro and Patrick Wu (1993). "Rheology of the upper mantle: A synthesis". In: *Science* 260.5109, pp. 771–778. DOI: 10.1126/science.260.5109.771.

Karlstrom, Leif, Scott R. Paterson, and A. Mark Jellinek (2017). "A reverse energy cascade for crustal magma transport". In: *Nature Geoscience* 10.8, pp. 604–608. DOI: 10.1038/NGEO2982.

Karlstrom, Leif and Mark Richards (2011). "On the evolution of large ultramafic magma chambers and timescales for flood basalt eruptions". In: *Journal of Geophysical Research: Solid Earth* 116.8, pp. 1–13. DOI: 10.1029/2010JB008159.

Kaula, William M. (1963). "Tidal dissipation in the Moon". In: *Journal of Geophysical Research* 68.17, pp. 4959–4965. DOI: 10.1029/jz068i017p04959.

Khurana, Krishan K., Xianzhe Jia, Margaret G. Kivelson, Francis Nimmo, Gerald Schubert, and Christopher T. Russell (2011). "Evidence of a global magma ocean in io's interior". In: *Science* 332, pp. 1186–1190. DOI: 10.1126/science.1201425.

Kirchoff, Michelle R. and William B. McKinnon (2009). "Formation of mountains on Io: Variable volcanism and thermal stresses". In: *Icarus* 201.2, pp. 598–614. DOI: 10.1016/j.icarus.2009.02.006.

Kirchoff, Michelle R., William B. McKinnon, and Paul M. Schenk (2011). "Global distribution of volcanic centers and mountains on Io: Control by asthenospheric heating and implications for mountain formation". In: *Earth and Planetary Science Letters* 301.1-2, pp. 22–30. DOI: 10.1016/j.epsl.2010.11.018.

Kleer, Katherine de et al. (2019). "Tidal Heating: Lessons from Io and the Jovian System". In: *KISS report*.

Klimczak, Christian, Kelsey T. Crane, Mya A. Habermann, and Paul K. Byrne (2018). "The spatial distribution of Mercury's pyroclastic activity and the relation to lithospheric weaknesses". In: *Icarus* 315.April 2017, pp. 115–123. DOI: 10.1016/j.icarus.2018.06.020.

Lainey, Valéry, Jean Eudes Arlot, Özgür Karatekin, and Tim Van Hoolst (2009). "Strong tidal dissipation in Io and Jupiter from astrometric observations". In: *Nature* 459.7249, pp. 957–959. DOI: 10.1038/nature08108.

Leconte, Jérémy (2018). "Continuous reorientation of synchronous terrestrial planets due to mantle convection /704/445/862 /704/445/210 /129 article". In: *Nature Geoscience* 11.3, pp. 168–172. DOI: 10.1038/s41561-018-0071-2.

Lister, John R. and Ross C. Kerr (1991). "Fluid-mechanical models of crack propagation and their application to magma transport in dykes". In: *Journal of Geophysical Research* 96.B6, pp. 10049–10077. DOI: 10.1029/91JB00600.

Lopes, Rosaly M. C. and T. K. P. Gregg (2004). *Volcanic worlds: Exploring the solar system's volcanoes*. Springer.

Lord, Peter et al. (2017). "Psyche: Journey to a Metal World". In: *IEEE Aerospace Conference Proceedings* 2014, pp. 1–11. DOI: 10.1109/AERO.2017.7943771.

Lu, Xinli and Susan W. Kieffer (2009). "Thermodynamics and Mass Transport in Multicomponent, Multiphase H2O Systems of Planetary Interest". In: *Annual Review of Earth and Planetary Sciences* 37.1, pp. 449–477. DOI: 10.1146/annurev.earth.031208.100109.

Macdonald, Gordon J F (1964). "Tidal Friction". In: *Reviews of Geophysics* 2.3. DOI: 10.1029/rg002i003p00467.

Manga, M. and C. Y. Wang (2007). "Pressurized oceans and the eruption of liquid water on Europa and Enceladus". In: *Geophysical Research Letters* 34.7, pp. 1–5. DOI: 10.1029/2007GL029297.

Matter, Alexis, Marco Delbo, Benoit Carry, and Sebastiano Ligori (2013). "Evidence of a metal-rich surface for the Asteroid (16) Psyche from interferometric observations in the thermal infrared". In: *Icarus* 226.1, pp. 419–427. DOI: 10.1016/j.icarus.2013.06.004. arXiv: 1306.2455.

McEwen, Alfred S., Laszlo P. Keszthelyi, Rosaly Lopes, Paul M. Schenk, and John R. Spencer (2004). "The lithosphere and surface of Io". In: *Jupiter. The planet, satellites and magnetosphere*. Ed. by Fran Bagenal, Timothy E Dowling, and William B Mckinnon. Cambridge, UK: Cambridge University Press, pp. 307–328.

Melosh (1989). *Impact Cratering, a geologic process*. New York, United States.

Moore, J. M., W. B. McKinnon, J. R. Spencer, A. D. Howard, P. M. Shenk, R. A. Beyer, F. Nimmo, and K. N. Singer (2016). "The geology of Pluto and Charon through the eyes of New Horizons". In: *Science* 351.6279. DOI: 10.1126/science.aad7055.

Moore, Jeffrey M. and Robert T. Pappalardo (2011). "Titan: An exogenic world?" In: *Icarus* 212.2, pp. 790–806. DOI: 10.1016/j.icarus.2011.01.019.

Moore, W. B. (2003). "Tidal heating and convection in Io". In: *Journal of Geophysical Research E: Planets* 108.8, pp. 1–6. DOI: 10.1029/2002je001943.

Moore, William B. (2001). "The thermal state of Io". In: *Icarus* 154.2, pp. 548–550. DOI: 10.1006/icar.2001.6739.

Moore, William B. and Gerald Schubert (2000). "The Tidal Response of Europa". In: *Icarus* 147.1, pp. 317–319. DOI: 10.1006/icar.2000.6460.

Murray, Carl D. and Stanley F. Dermott (1999). *Solar System Dynamics*. New York, United States: Camb. DOI: 10.1017/cbo9781139174817.

Neeley, J. R., B. E. Clark, M. E. Ockert-Bell, M. K. Shepard, J. Conklin, E. A. Cloutis, S. Fornasier, and S. J. Bus (2014). "The composition of M-type asteroids II: Synthesis of spectroscopic and radar observations". In: *Icarus* 238, pp. 37–50. DOI: 10.1016/j.icarus.2014.05.008.

Neufeld, Jerome A, James F.J. Bryson, and Francis Nimmo (2019). "The top-down solidification of iron asteroids driving dynamo evolution. In prep." In: pp. 1–62.

Nimmo, F., B. G. Bills, and P. C. Thomas (2011). "Geophysical implications of the long-wavelength topography of the Saturnian satellites". In: *Journal of Geophysical Research E: Planets* 116.11, pp. 1–12. DOI: 10.1029/2011JE003835.

Nimmo, F., B. G. Bills, P. C. Thomas, and S. W. Asmar (2010). "Geophysical implications of the long-wavelength topography of Rhea". In: *Journal of Geophysical Research E: Planets* 115.10, pp. 1–11. DOI: 10.1029/2010JE003604.

Nimmo, F. and J. R. Spencer (2015). "Powering Triton's recent geological activity by obliquity tides: Implications for Pluto geology". In: *Icarus* 246.C, pp. 2–10. DOI: 10.1016/j.icarus.2014.01.044.

Nimmo, F., P. C. Thomas, R. T. Pappalardo, and W. B. Moore (2007). "The global shape of Europa: Constraints on lateral shell thickness variations". In: *Icarus* 191.1, pp. 183–192. DOI: 10.1016/j.icarus.2007.04.021.

Ojakangas, Gregory W. and David J. Stevenson (1989). "Thermal State of an Ice Shell on Europa". In: *Icarus* 81.2, pp. 220–241. DOI: 10.1016/0019-1035(89)90052-3.

Pappalardo, Robert T. et al. (2019). "The Europa Clipper: Science and Mission". In: *AGU Fall Meeting*, P53B–06.

Perry, Mark E. et al. (2015). "The low-degree shape of Mercury". In: *Geophysical Research Letters* 42.17, pp. 6951–6958. DOI: 10.1002/2015GL065101.

Petford, Nick, John R. Lister, and Ross C. Kerr (1994). "The ascent of felsic magmas in dykes". In: *Lithos* 32.1-2, pp. 161–168. DOI: 10.1016/0024-4937(94)90028-0.

Porco, Author C C et al. (2006). "Cassini observes the active south pole of Enceladus". In: 311.March, pp. 1393–1401. DOI: 10.1126/science.1123013.

Retherford, K D et al. (2015). "The Ultraviolet Spectrograph on the Europa Mission (Europa-UVS)". In: *AGU Fall Meeting Abstracts*. Vol. 2015, P13E–02.

Roberts, James H. and Francis Nimmo (2008). "Tidal heating and the long-term stability of a subsurface ocean on Enceladus". In: *Icarus* 194.2, pp. 675–689. DOI: 10.1016/j.icarus.2007.11.010.

Ross, Martin and Gerald Schubert (1986). "Tidal Dissipation in a Viscoelastic Planet". In: *Lunar and Planetary Science Conference*, pp. 447–452.

Roth, Lorenz, Joachim Saur, Kurt D. Retherford, Darrell F. Strobel, Paul D. Feldman, Melissa A. McGrath, and Francis Nimmo (2014). "Transient water vapor at Europa's south pole". In: *Science* 343.6167, pp. 171–174. DOI: 10.1126/science.1247051.

Rubin, Allan M. (1995). "Propagation of Magma-Filled Cracks". In: *Annual Reviews*, pp. 215–217.

Rubin, Allan M (1998). "Dike ascent in partially molten rock". In: *Journal of Geophysical Research: Solid Earth* 103, pp. 20901–20919. DOI: 10.1029/98JB01349.

Ruesch, Ottaviano, Antonio Genova, Wladimir Neumann, Lynnae C. Quick, Julie C. Castillo-Rogez, Carol A. Raymond, Christopher T. Russell, and Maria T. Zuber (2019). "Slurry extrusion on Ceres from a convective mud-bearing mantle". In: *Nature Geoscience* 12.7, pp. 505–509. DOI: 10.1038/s41561-019-0378-7.

Sabadini, Roberto and Bert Vermeersen (2004). *Global Dynamics of the Earth*. Springer Dordrecht. DOI: 10.1007/978-94-017-1709-0.

Sagan, Carl (1979). "Sulphur flows on Io". In: *Nature* 280, pp. 750–753. DOI: 10.1038/280750a0.

Scanlan, Kirk M., Cyril Grima, Gregor Steinbrügge, Scott D. Kempf, Duncan A. Young, and Donald D. Blankenship (2019). "Geometric determination of ionospheric total electron content from dual frequency radar sounding measurements". In: *Planetary and Space Science* 178.June, p. 104696. DOI: 10.1016/j.pss.2019.07.010.

Scheinberg, A., L. T. Elkins-Tanton, G. Schubert, and D. Bercovici (2016). "Core solidification and dynamo evolution in a mantle-stripped planetesimal". In: *Journal of Geophysical Research: Planets* 121.1, pp. 2–20. DOI: 10.1002/2015JE004843.

Schenk, Paul M., William B. McKinnon, David Gwynn, and Jeffrey M. Moore (2001). "Flooding of Ganymede's bright terrains by low-viscosity water-ice lavas". In: *Nature* 410.6824, pp. 57–60. DOI: 10.1038/35065027.

Shepard, Michael K et al. (2017). "Radar observations and shape model of asteroid 16 Psyche". In: *Icarus* 281, pp. 388–403. DOI: https://doi.org/10.1016/j.icarus.2016.08.011.

Sori, Michael M. (2018). "A thin, dense crust for Mercury". In: *Earth and Planetary Science Letters* 489, pp. 92–99. DOI: 10.1016/j.epsl.2018.02.033.

Steinbrügge, G., D. M. Schroeder, M. S. Haynes, H. Hussmann, C. Grima, and D. D. Blankenship (2018). "Assessing the potential for measuring Europa's tidal Love number h2 using radar sounder and topographic imager data". In: *Earth and Planetary Science Letters* 482.2018, pp. 334–341. DOI: 10.1016/j.epsl.2017.11.028.

Tkalcec, B. J., G. J. Golabek, and F. E. Brenker (2013). "Solid-state plastic deformation in the dynamic interior of a differentiated asteroid". In: *Nature Geoscience* 6.2, pp. 93–97. DOI: 10.1038/ngeo1710.

Tsai, Victor C. and David J. Stevenson (2007). "Theoretical constraints on true polar wander". In: *Journal of Geophysical Research: Solid Earth* 112.5, pp. 1–10. DOI: 10.1029/2005JB003923.

Turcotte, D L and Gerald Schubert (2014). *Geodynamics*. Cambridge, England: Cambridge University Press.

Turtle, E. P. et al. (2019). "The Europa Imaging System (EIS): High-Resolution, 3-D Insight into Europa's Geology, Ice Shell, and Potential for Current Activity". In: *Lunar and Planetary Science Conference*. Lunar and Planetary Science Conference, p. 3065.

Tyler, Robert H., Wade G. Henning, and Christopher W. Hamilton (2015). "TIDAL HEATING in A MAGMA OCEAN WITHIN JUPITER'S MOON Io". In: *Astrophysical Journal, Supplement Series* 218.2, p. 22. DOI: 10.1088/0067-0049/218/2/22.

Wahr, J. M., M. T. Zuber, David E. Smith, and J. I. Lunine (2006). "Tides on Europa, and the thickness of Europa's icy shell". In: *Journal of Geophysical Research E: Planets* 111.12, pp. 1–10. DOI: 10.1029/2006JE002729.

Wasson, John T. (1985). *Meteorites: Their record of early solar-system history*. New York, United States: W. H. Freeman Press, p. 267.

Williams, David A., Ronald Greeley, Rosaly M.C. Lopes, and Ashley G. Davies (2001). "Evaluation of sulfur flow emplacement on Io from Galileo data and numerical modeling". In: *Journal of Geophysical Research E: Planets* 106.E12, pp. 33161–33174. DOI: 10.1029/2000JE001340.

Williams, Quentin (2009). "Bottom-up versus top-down solidification of the cores of small solar system bodies: Constraints on paradoxical cores". In: *Earth and Planetary Science Letters* 284.3-4, pp. 564–569. DOI: 10.1016/j.epsl.2009.05.019.

Wilson, Lionel (2009). "Volcanism in the solar system". In: *Nature Geoscience* 2.6, pp. 389–397. DOI: 10.1038/ngeo529.

Wilson, Lionel and James W. Head (2017). "Generation, ascent and eruption of magma on the Moon: New insights into source depths, magma supply, intrusions and effusive/explosive eruptions (Part 1: Theory)". In: *Icarus* 283.2017, pp. 146–175. DOI: 10.1016/j.icarus.2015.12.039.

Yang, Jijin, Joseph I Goldstein, and Edward R D Scott (2008). "Metallographic cooling rates and origin of IVA iron meteorites". In: *Geochimica et Cosmochimica Acta* 72, pp. 3042–3061. DOI: 10.1016/j.gca.2008.04.009.

Yang, Jijin, Joseph I. Goldstein, and Edward R.D. Scott (2007). "Iron meteorite evidence for early formation and catastrophic disruption of protoplanets". In: *Nature* 446.7138, pp. 888–891. DOI: 10.1038/nature05735.

Zschau, J. (1978). "Tidal Friction in the Solid Earth: Loading Tides Versus Body Tides". In: *Tidal Friction and the Earth's Rotation*, pp. 62–94.

Appendix A

Appendix to Europa Chapter

Computing $\underline{\boldsymbol{A}}$

To compute A_{ij} we begin with the fact that the topography at any point (θ, ϕ) is given, in spherical harmonics, by

$$h = \sum_{l,m=0}^{\infty} C_{lm} \cos(m\phi) P_{lm}(\cos\theta) + S_{lm} \sin(m\phi) P_{lm}(\cos\theta)$$

. If our measurements were topographic points, rather than chords, computing $\underline{\boldsymbol{A}}$ would be simple. For example, $A_{23} = \frac{\partial z_2}{\partial x_3} = \frac{\partial z_2}{\partial C_{11}} = \cos(\phi) P_{11}(\cos\theta)$ which, crucially, contains no elements of $\hat{\boldsymbol{x}}$ so $\hat{\boldsymbol{x}}$ can be calculated without assuming it a priori. However, because our measurements are chords, we need to get the chord length itself in terms of spherical harmonics. The chord length between two surface points h_1 and h_2 follows from treating them as a triangle with the angle between them γ. The law of cosines gives us the length, $c = \sqrt{h_1^2 + h_2^2 - 2h_1 h_2 \cos\gamma}$. Trying to compute an element of A reveals our problem

$$\frac{\partial c_i}{\partial C_{lm}} = \frac{\partial c_i}{\partial h_{i1}} \frac{\partial h_{i1}}{\partial C_{lm}} + \frac{\partial c_i}{\partial h_{i2}} \frac{\partial h_{i2}}{\partial C_{lm}} \tag{A.1}$$

$$= \frac{h_{i1} - h_{i2}\cos\gamma}{c_i} \cos(m\phi_{i1}) P_{lm}(\cos\theta_{i1}) + \frac{h_{i2} - h_{i1}\cos\gamma}{c_i} \cos(m\phi_{i2}) P_{lm}(\cos\theta_{i2}) \tag{A.2}$$

In general, the terms in fractions in equation A.2 inherently depend on the spherical harmonics we are trying to fit. This means that it is impossible to compute elements of $\underline{\boldsymbol{A}}$ which are independent of $\hat{\boldsymbol{x}}$ and thus allow us to solve for $\hat{\boldsymbol{x}}$. One solution to this is to solve $\hat{\boldsymbol{x}}$ iteratively, beginning with an assumed shape $\hat{\boldsymbol{x}}_0$, using this to compute a new $\hat{\boldsymbol{x}}_1$, and repeating until the result converges. This approach has the advantage of being clear when a self consistent result is found. Another approach is to note that for a hydrostatic planet (like Europa), topography is a small perturbation on the overall radius and we can assume $h_1 \approx h_2 \approx R$, the planet's radius. Then, a bit of trigonometry tells us that $\frac{h_1 - h_2 \cos\gamma}{c} \approx \frac{R(1-\cos\gamma)}{2R\sin\frac{\gamma}{2}} = \sin\frac{\gamma}{2}$, and γ is calculable from $(\theta_1, \phi_1, \theta_2, \phi_2)$. This assumption, that $h_1 \approx h_2 \approx R$, allows us to calculate $\underline{\boldsymbol{A}}$ independent of $\hat{\boldsymbol{x}}$, as

$$A_{ij} = \frac{\partial c_i}{\partial C_{lm}} = \frac{\partial c_i}{\partial h_{i1}} \frac{\partial h_{i1}}{\partial C_{lm}} + \frac{\partial c_i}{\partial h_{i2}} \frac{\partial h_{i2}}{\partial C_{lm}} \tag{A.3}$$

$$= \sin\frac{\gamma_i}{2} \Big[\cos(m\phi_{i1}) P_{lm}(\cos\theta_{i1}) + \cos(m\phi_{i2}) P_{lm}(\cos\theta_{i2}) \Big] \tag{A.4}$$

Note that this assumed z_i was a C_{lm} term and not an S_{lm} term, but the result in the latter case just swaps $\sin(m\phi)$ for $\cos(m\phi)$

Appendix B

Appendix to Io Rotation

B.1 Goldreich and Mitchell algebra

Goldreich and Mitchell (2010) compute eccentricity tides on a decoupled shell, their equation 16

$$T_{G\&M} = \frac{576}{5}\pi\left(\frac{1+\nu}{5+\nu}\right)\frac{h_t^2}{Q}(qe)^2\mu d R^2 \tag{B.1}$$

This is using their notation. Comparing this, the result for a decoupled shell, to our results for a coherent body, is easiest if we can compare it to the solution from Correia et al. (2014). As we used in our Equation 3.1 say

$$T_{Correia} = -\frac{3Gm_0^2R^5}{2a^6}\sum_{k=-\infty}^{\infty}\left(X_k^{-3,2}(e)\right)^2 k_2(\omega_k)\sin\left(\delta(\omega_k)\right) \tag{B.2}$$

Although the notations are very different, these two equations turn out to be almost identical.

Manipulating the Goldreich and Mitchell (2010) equation first, we introduce and then divide by their $\mathcal{R}$ factor, that describes the relative importance of elasticity and gravity.

$$\mathcal{R} \equiv \frac{E_{elas}}{E_{grav}} = \frac{32\pi}{5}\left(\frac{1+\nu}{5+\nu}\right)\frac{(1+k_f)^2}{k_f}\frac{\mu d R^3}{GM^2} \tag{B.3}$$

$$\frac{T_{G\&M}}{\mathcal{R}} = \frac{\frac{576}{5}\pi\left(\frac{1+\nu}{5+\nu}\right)\frac{h_t^2}{Q}(qe)^2\mu d R^2}{\frac{32\pi}{5}\left(\frac{1+\nu}{5+\nu}\right)\frac{(1+k_f)^2}{k_f}\frac{\mu d R^3}{GM^2}} \tag{B.4}$$

$$= \frac{18\frac{h_t^2}{Q}(qe)^2}{\frac{(1+k_f)^2}{k_f}\frac{R}{GM^2}} \tag{B.5}$$

$$T_{G\&M} = 18\frac{h_t^2}{Q}(qe)^2\frac{k_f}{(1+k_f)^2}\frac{GM^2}{R}\mathcal{R} \tag{B.6}$$

Note that in their notation k_t is equivalent to our $k_2(n)$ and k_f is equivalent to $k_2(0) \approx k_2(\omega_{\text{NSR}})$ (and similarly for h_2). Their Q is not explicitly frequency dependent, but can be interpreted as the tidal frequency $Q(n)$.

Like we did in the main text, we expand $T_{Correia}$ to second order in e, but this time don't set it equal to zero. Instead we calculate it for synchronous rotation to match Goldreich and Mitchell (2010), which means that the $k = 2$ (index in the sum, not love number) term is zero.

$$T_{Correia} \approx -\frac{3Gm_0^2R^5}{2a^6}\sum_{k=1}^{3}\left(X_k^{-3,2}(e)\right)^2 k_2(\omega_k)\sin\left(\delta(\omega_k)\right) \tag{B.7}$$

$$= -\frac{3Gm_0^2R^5}{2a^6}\left(\frac{1}{4}e^2\frac{k_2(n)}{Q(n)} - \frac{49}{4}e^2\frac{k_2(n)}{Q(n)}\right) \tag{B.8}$$

$$= \frac{18Gm_0^2R^5}{a^6}e^2\frac{k_2(n)}{Q(n)} \tag{B.9}$$

Then returning to the Goldreich and Mitchell (2010) version, we note that $q = \frac{n^2R^3}{GM} = \frac{R^3}{GM}\frac{Gm_0}{a^3} = \frac{R^3}{a^3}\frac{m_0}{M}$ and that $1 + k_f \approx h_f$.

$$T_{G\&M} = \frac{18Gm_0^2R^5}{a^6}e^2\frac{h_t^2}{h_f^2}\frac{k_f}{Q}\mathcal{R} \tag{B.10}$$

$$T_{G\&M} = T_{Correia}\frac{k_f}{h_f^2}\frac{h_t^2}{k_t}\mathcal{R} \tag{B.11}$$

So we see that Goldreich and Mitchell (2010)'s solution for the net torque on a synchronous shell is almost identical to Correia's solution for the torque on the whole body.

Taking this at face value, we assume that if (Goldreich and Mitchell 2010) had kept higher order terms, they would enter similarly, so we keep k_f and h_f as-is but replace k_t and h_t with the general frequency-dependent $k_2(\omega_k)$ and $h_2(\omega_k)$. We also note that $\mathcal{R}$ is frequency dependent, so we make that dependence explicit through the fact that d, the elastic thickness, is frequency dependent (see below). Then we can write a (Goldreich and Mitchell 2010) equivalent of the (Correia et al. 2014) equation but for a decoupled shell:

$$T_{Correia} = -\frac{3Gm_0^2R^5}{2a^6}\sum_{k=-\infty}^{\infty}\left(X_k^{-3,2}(e)\right)^2 k_2(\omega_k)\sin\left(\delta(\omega_k)\right) \tag{B.12}$$

$$\implies T_{G\&M} = -\frac{3Gm_0^2R^5}{2a^6}\sum_{k=-\infty}^{\infty}\frac{k_f}{h_f^2}\frac{h_2(\omega_k)^2}{k_2(\omega_k)}\mathcal{R}(\omega_k)\left(X_k^{-3,2}(e)\right)^2 k_2(\omega_k)\sin\left(\delta(\omega_k)\right) \tag{B.13}$$

$$= -\frac{3Gm_0^2R^5k_f}{2a^6h_f^2}\sum_{k=-\infty}^{\infty}h_2(\omega_k)^2\mathcal{R}(\omega_k)\left(X_k^{-3,2}(e)\right)^2\sin\left(\delta(\omega_k)\right) \tag{B.14}$$

Then we can solve for when this equals zero like we did in Equation 3.4

$$\frac{h_2^2(2\omega_{\rm NSR})}{Q(2\omega_{\rm NSR})}\mathcal{R}(2\omega_{\rm NSR}) = 12e^2\frac{h_2^2(n)}{Q(n)}\mathcal{R}(n) \tag{B.15}$$

$$\frac{h_2(2\omega_{\rm NSR})}{Q(2\omega_{\rm NSR})} = 12e^2\frac{h_2(n)}{Q(n)}\frac{\mathcal{R}(n)}{\mathcal{R}(2\omega_{\rm NSR})}\frac{h_2(n)}{h_f} \tag{B.16}$$

$$\frac{h_2(2\omega_{\rm NSR})}{Q(2\omega_{\rm NSR})} = 12e^2\frac{h_2(n)}{Q(n)}\frac{d(n)}{d(2\omega_{\rm NSR})}\frac{h_2(n)}{h_f} \tag{B.17}$$

$$\frac{h_2(2\omega_{\rm NSR})}{Q(2\omega_{\rm NSR})} = 12e^2\frac{h_2(n)}{Q(n)}\frac{50}{\ln\left(\frac{n}{\omega_{\rm NSR}}\right)}\frac{h_2(n)}{h_f} \tag{B.18}$$

and the differences are fairly minor. The k_2s are replaced by h_2s and are squared in Equation B.15 so we can pull them out for Equation B.16 (noting that $h_2(\omega_{\rm NSR}) \approx h_f$) and see that our result is almost the same as in Equation 3.4, and the necessary $\frac{h_2(\omega_{\rm NSR})}{Q_{NSR}}$ is reduced by a factor of $\frac{h_2(n)}{h_f}\frac{50}{\ln\left(\frac{n}{\omega_{\rm NSR}}\right)}$.

The step from Equation $B.16$ to Equation $B.17$ is because we include the frequency dependence of $\mathcal{R}$, the relative importance of elasticity and self gravity, through the elastic thickness d. Io's lithosphere has a temperature gradient with depth, which means there is a

viscosity gradient with depth. The brittle-ductile transition, the depth below which material will not have elastic strength, depends on both viscosity and frequency, so the effective thickness of Io's lithosphere is frequency dependent. Because viscosity is exponential in temperature, we can take an order of magnitude approach to temperature and get a sufficiently precise result.

Io's mean surface temperature is 120 K. The viscosity of rock can be described as (Karato and Wu 1993)

$$\eta = \eta_0 e^{\frac{E_a}{RT}} \tag{B.19}$$

$$\implies \frac{\eta_n}{\eta_{\omega_{\rm NSR}}} = e^{\frac{E_a}{RT_n} - \frac{E_a}{RT_{\omega_{\rm NSR}}}} \tag{B.20}$$

$$\frac{\omega_{\rm NSR}}{n} \approx e^{\frac{E_a}{Rd_n \frac{\partial T}{\partial z}} - \frac{E_a}{Rd_{\omega_{\rm NSR}} \frac{\partial T}{\partial z}}} \tag{B.21}$$

$$\frac{\omega_{\rm NSR}}{n} \approx e^{\frac{E_a}{RT_{base} \frac{d_n}{d_{\omega_{\rm NSR}}}} - \frac{E_a}{RT_{base}}} \tag{B.22}$$

$$\frac{\omega_{\rm NSR}}{n} \approx e^{\frac{E_a}{RT_{base}} \left(1 - \frac{d_{\omega_{\rm NSR}}}{d_n}\right)} \tag{B.23}$$

$$\frac{\omega_{\rm NSR}}{n} \approx e^{50 \left(1 - \frac{d_{\omega_{\rm NSR}}}{d_n}\right)} \tag{B.24}$$

$$\frac{1}{50} \ln\left(\frac{\omega_{\rm NSR}}{n}\right) \approx 1 - \frac{d_{\omega_{\rm NSR}}}{d_n} \approx -\frac{d_{\omega_{\rm NSR}}}{d_n} \tag{B.25}$$

$$\frac{1}{50} \ln\left(\frac{n}{\omega_{\rm NSR}}\right) \approx \frac{d_{\omega_{\rm NSR}}}{d_n} \tag{B.26}$$

We used an activation energy of 300 kJ/mol for olivine, and assumed the long-period brittle-ductile transition is about 800 K (half the melting point). Note that the approximation in equation B.26 is pretty rough. Because this is only an approximate calculation, we ignore this order-unity error, but it is the most significant approximation in this calculation.

B.2 Testing Multiple Layers

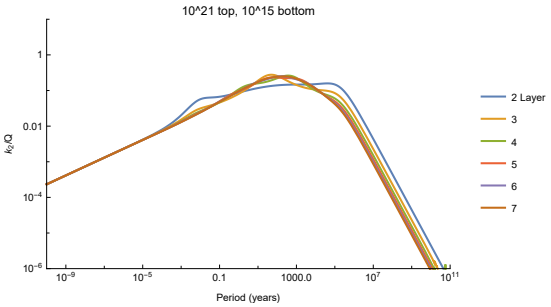

Figure B.1: Testing the effect of having many layers. These models all have exponential viscosity profiles with depth, with viscosities of 10^{15} Pa·s at the center and 10^{21} Pa·s at the surface. Two layers means the deeper half of the body (by radius) is 10^{15} Pa·s and the surface half is 10^{21} Pa·s, three layers means the middle third is 10^{18} Pa·s, and so on. We see the long period tail shift slightly with more layers, but overall the behavior is very similar.